ide A n le ma in Lidar   A L   eployment at the A   outhern

reat Plains ite   nter omparison of Cloud Property   etrievals

gor . Polonsky, Ste en P. Lo e, and Anthony B. Da is

Los Alamos   ational Laboratory,

Space and Remote Sensing Sciences Group (SR -2),

MS-436, Los Alamos,   M 7545,   SA

Corresponding author address: gor   . Polonsky

Los Alamos   ational Laboratory

Space and Remote Sensing Sciences Group (SR -2),

MS-436, Los Alamos,   M 7545,   SA

E :mail: polonsky lanl.go

Abstract

The Wide-Angle Imaging Lidar (WAIL), a new instrument that measures cloud optical and geometrical properties by means of off-beam lidar returns, was deployed as part of a multi-instrument campaign to probe a cloud field at ARM (Atmospheric Radiation Measurement) Southern Great Plain (SGP) site on March 25, 2002. WAIL is designed to determine physical and geometrical characteristics using the off-beam component of the lidar return that can be adequately modeled within the diffusion approximation. Using WAIL data, we estimate the extinction coefficient and *geometrical* thickness of a dense cloud layer; from there, we infer *optical* thickness. Results from the new methodology agree well with counterparts obtained from other instruments located permanently at the SGP ARM site and from the WAIL-like airborne instrument that flew over the site during our observation period.

a round and utline

The term "lidar" has traditionally implied a ranging device, the basic idea being to send out a pulse of light and then to detect returns from objects of interest. The importance of this concept is such that it contributes to the acronym LIDAR (LIght Detection And Ranging). The assumption of one-to-one correspondence between the object location and the instant at which the pulse has returned enables the probing of the inner structure of the medium. Many artificial and natural objects are now investigated using lidar techniques. Even limiting ourselves to monostatic backscattering lidar, we can list seawater, aerosol, optically thin clouds (such as cirrus), natural and artificial fogs, pollution, and smoke.

Conversion of photon travel time to range mandates that contributions from multiple scattering be neglected or somehow discriminated. Largely for this reason, backscatter lidar receivers are generally designed with as narrow a field of view (FOV) as possible, in order to restrict the backscattered light to small angles around the transmitted beam's direction. This portion of multiple scattering arising from small-angle scattering has been successfully modeled [Zege et al., 1994, Bissonnette, 1996], and used to obtain extra information about the probed object [Bissonnette et al., 2002]. But for optically thick objects such as dense clouds, the on-beam or even small-angle signal quickly becomes contaminated by a multiple-scattering component which cannot be associated with a particular location inside the cloud. In this case, all ranging information beyond detection of the cloud boundary (ceilometry) is irretrievably lost.

This fundamental difficulty can be overcome by a radically different technique called "off-beam lidar," first suggested by Davis et al. [1997a;b]. Here, instead of restricting the receiver's FOV to reject multiply-scattered light, it is made as wide as possible in order to collect essentially all of the multiply-scattered returning light. An even more radical departure from

the basic idea of lidar remote sensing was recently proposed by Evans [2003] where both the transmitter and the receiver are in fact *inside* the sounded cloud; they call this concept for an airborne platform "in-situ" cloud lidar where there is nothing left of the ranging, only multiple-scattering counts. To make use of the information contained in these off-beam signals, we need a completely new lidar equation.

The principle of off-beam lidar is predicated on the fact that multiple scattering thoroughly samples the interior of the medium. So the characteristics of the reflected radiance distribution in space, angle and time will depend on its optical and geometrical properties. Photons should be collected within a receiver FOV wide enough to take in essentially the entire spatial distribution of the reflected radiance at the medium boundary, and this should enable the retrieval of both geometrical thickness H and a volume-averaged extinction coefficient σ (equivalently, the mean optical depth $\tau = \sigma H$). Figure 1 illustrates schematically cloud observation with a ground-based off-beam lidar while Table 1 describes the key variables and parameters.

Using scaling arguments from random walk (i.e., phenomenological diffusion) theory, Davis et al. [1997b] showed that the mean value of t, the time spent by the laser photons inside the cloud before escaping in reflection, is given by

$$\langle t \rangle \propto H/c \tag{1}$$

where c is the velocity of light, while the root-mean-square (RMS) lateral transport distance r between the laser beam and the escape position is given by

$$\sqrt{\langle r^2 \rangle} \propto H/\sqrt{(1-g)\tau} \tag{2}$$

where g is the asymmetry factor (≈ 0.85 for the dense liquid clouds of interest here). Equation (2) shows that the size of the remotely observable light field excited by the laser, all times considered, is a relatively weak function of optical depth. It is essentially commensurate with

cloud thickness. This immediately sets lower bounds on the fields-of-regard for off-beam lidar devices: $\approx 60°$ for a ground-based system looking at a cloud that is ≈ 1 km thick and ≈ 1 km high; no less than $\approx 6°$ for an airborne system looking at the same low-level cloud from about 10 km altitude.

Bypassing the derivation by Davis et al. [1997b], one can see that (1) is equivalent to the often repeated but seldom proven statement that the (typical) number of scatterings for reflected light goes as optical depth. Indeed, multiplying both sides of (1) by σc we see that $\langle \sigma ct \rangle$, mean *optical* path inside the cloud (which is incremented by unity at each scattering), is proportional to $\sigma H = \tau$. Physically speaking, there is an expanding "cloud" of photons spreading into the cloudy medium at a rate that would be given by the classic law of diffusion [Einstein, 1905]:

$$\langle r^2 \rangle = Dt \qquad (3)$$

were it not for cloud boundary effects. $D = c\ell_t/3$ denotes photon diffusivity which depends only on the "transport" mean-free-path $\ell_t = 1/(1-g)\sigma$. Using (1) to determine t in (3), as a rough estimate of when photons return to the illuminated boundary, yields $\langle r^2 \rangle \approx \ell_t H$ which is equivalent to (2). Davis et al. [1999] used rigorous diffusion theory in finite media to improve the basic off-beam lidar relations in (1)–(2), thus providing exact $O(1)$ proportionality constants and correction terms dependent on $(1-g)\tau$. These corrections are not insignificant in the observed range of τ. In all of this photon absorption is assumed inconsequential which is why the diffuse radiance field excited by the pulsed laser on one boundary can permeate the whole cloud, and thus be exploited as suggested in (1) and (2) to extract H and τ.

Off-beam lidar can therefore compete with mm-radar as a probe of cloud structure in the sense of height, thickness and density. It will of course not yield the same spatial detail as mm-radar since lidar-based estimates of H and τ are be inherently averaged over a horizontal scale

5

commensurate with (2), nor is detailed stratification information available. (We discuss ways of inferring internal cloud variability from off-beam signal analysis in our closing remarks, and the ability of off-beam lidar to detect more than one cloud layer has yet to be determined.) In mm-radar, reflectivity is however weighted towards the largest droplets. It responds therefore very strongly to drizzle. So much in fact that radiative and microphysical quantities of interest in climate studies, including the lower cloud boundary, are all but lost [Clothiaux et al., 1995]. We view off-beam lidar as a natural extension of on-beam lidar and as a complement to mm-radar at a visible wavelength that bears directly on the climatic impact of clouds.

It is interesting to recall here the venerable history of using steady-state diffusion theory in cloud remote sensing. Indeed, Meador and Weaver [1980] showed that all 2-stream approximations in atmospheric radiative transfer theory are mathematical variants of the 1D diffusion equation which was first solved in this context by Schuster [1905]. As an example germane to the ground-based remote-sensing of clouds, the methodology advanced by Min and Harrison [1996] is ultimately based on diffusion theory, as is most cloud remote sensing in the solar spectrum. Operational implementation of techniques based on multi-stream solutions of the 1D radiative transfer problem are indeed a relatively recent development, e.g., Nakajima and King [1990]. Outside of off-beam and in-situ lidars, the last conscious effort to exploit diffusion theory in a new cloud-probing instrument we know about is by King [1986]. Their Cloud Absorption Radiometer was designed for airborne in-cloud operation and successfully deployed by King et al. [1990] in a marine stratocumulus layer. As anticipated, these authors found the characteristic angular signature of diffusion in dense clouds wich later motivated the phenomenology of radiative smoothing [Cahalan et al., 1989, Marshak et al., 1995, Davis et al., 1997a]. Radiative smoothing theory, which is ultimately based on (2), not only contributed to finding the resolution (satellite pixel size) and other conditions at which the modeling error in

cloud remote sensing due to the 1D assumption is at a minimum but also lead to the concept of off-beam lidar [Davis et al., 1997a].

Davis [1999] extended the temporal scaling argument that yields (1) to show that

$$\langle t^2 \rangle \propto (1-g)\tau \times (H/c)^2, \tag{4}$$

a prediction confirmed and refined by the analytical diffusion theory of Davis et al. [1999]. Bringing together (1) and (4) demonstrates that H and τ can in principle be derived from temporal observations alone. This was independently verified by Miller et al. [1999] using detailed Monte Carlo results for space-borne lidar geometry while Davis et al. [2001] successfully applied their two-moment temporal method to data collected over clouds during the LIdar-in-space Technology Experiment (LITE). Furthermore, the time-domain retrieval method developed by Evans [2003] for in-situ cloud lidar confirms that waveforms alone contain enough information to infer cloud properties.

Inspired by the simple relations in (1)–(2) and (4), the first versions of the off-beam cloud lidar technique were based on estimation of the spatial and temporal moments of the radiance distribution. This assumes that these distributions are measured over a wide-enough range in t and r, maybe twice the values of the low-order moments in (1)–(2). As shown further on, this is not always possible. The theory was further developed by Polonsky and Davis [2004], allowing one to estimate analytically the corresponding distributions. We shall use these new formulas here to retrieve cloud properties even when the distributions are quite severely truncated in the observations.

The above scaling arguments provided a compelling rationale to create the first prototype of a ground-based off-beam lidar system. This device, called Wide-Angle Imaging Lidar or "WAIL," was deployed in field experiments near Los Alamos, NM [Love et al., 2001; 2002]. We thus demonstrated that, even with a relatively modest laser (0.5 mJ/pulse), reflected

7

radiance was readily detected with existing technology out to $\approx 30°$ off zenith for a 1 km cloud ceiling. We also showed that the moment-based retrieval algorithms for geometrical and optical thicknesses outlined above gave reasonable results. But lacking independent measurements of the cloud properties in those early experiments, the qualification of "reasonable" was based on visual assessment of the clouds of opportunity.

Here, for the first time, WAIL was deployed alongside other cloud-probing systems: a microwave radiometer [Liljegren, 1994], a mm-wave cloud radar [Moran et al., 1998], a ceilometer [Lonnqvist, 1995], and a micro-pulse lidar [?]. This suite of ARM instruments was used to sound an extensive cloud layer above the Oklahoma SGP site during the night of March 24-25, 2002, thus enabling a direct comparison of WAIL with other instruments. In addition to these ground-based instruments, another off-beam lidar system, THOR (THickness from Off-beam Returns), was looking down at the same cloud system from NASA's P-3 aircraft; THOR's design and performance are described by Cahalan et al. [2004]. For our present purposes, THOR's on-beam channel provided yet another estimate of cloud-top altitude although not immediately above head.

In this article we use recently developed diffusion theory by Polonsky and Davis [2004] to retrieve cloud parameters from WAIL data. The particular cloud field that prevailed during our joint observation period was less than ideal for WAIL in its current configuration: the ceiling was never above 0.5 km, so WAIL's 53.6° full-width FOV was insufficient to capture the entire spatial radiance pattern emanating from the relatively thick ($H \approx 0.5$-0.7 km) and opaque ($\tau \approx 15$-30) cloud. This handicap notwithstanding, the new theory still yields good retrievals from the truncated distributions.

In the following section we describe the WAIL instrument and compare the current version with a previous incarnation discussed in earlier papers. In Section 3, the required diffusion

theoretical results are surveyed without derivations but their accuracy is verified by comparison with detailed Monte Carlo simulations. Section 4 gives observational details about the March 2002 deployment at the ARM site in Oklahoma. Analyses of selected WAIL data from that collection are presented in Section 5, yielding estimates of cloud parameters. These retrievals are compared with independent estimates in Section 6. In Section 7, we summarize our findings and outline future work on the instrumental and theoretical aspects of off-beam lidar.

he A L nstrument ystem

WAIL is a fully imaging implementation of the off-beam lidar concept. The basic idea is to send a narrow-beam, short-pulse laser into a cloud, an excitation approximating a Dirac δ-function in both space and time, and to monitor the returning light at high temporal and spatial resolution. In essence, one collects a high-speed "movie" of the returning light which is, by definition, a physical manifestation of the cloud's Green function for the time-dependent radiative transfer equation. For ground-based measurements, this must be done over a very wide FOV, sufficient to take in a roughly kilometer-wide expanse of cloud, commensurate with the cloud layer's physical thickness. With cloud bases typically on the order of a kilometer above the ground, the required full-angle FOV is about one radian.

In earlier work [Love et al., 2001; 2002], we described a realization of WAIL based on a novel micro-channel-plate, crossed delay line (MCP/CDL) photon-counting imager developed at Los Alamos National Laboratory. This powerful new type of low-light imaging system was described in detail by Priedhorsky et al. [1996]. The MCP/CDL detector system's extremely high time resolution (100 ps) and excellent low-light sensitivity made it attractive for our prototype WAIL experiments, including some early laboratory-scale simulations of off-beam

lidar (100 ps corresponds to a path of only 3 cm), where the "cloud" was a moderate-sized aquarium filled with a scattering liquid suspension [Davis et al., 1998].

The MCP/CDL's main disadvantage for WAIL arises from its unique method of imaging. It relies upon accurately timing the photo-electron pulses, originating from individual photon impacts, that emerge from the two orthogonal delay lines. This timing-based imaging scheme becomes confused when flux over the entire detector exceeds roughly 5×10^6 photons/second, thus placing a firm upper limit on the amount of light that can admitted into the system. This constraint becomes problematical for off-beam lidar experiments on clouds, because of the orders-of-magnitude dynamic range between the bright initial return and the long-time and large-displacements returns of particular interest here.

We therefore developed a second implementation of WAIL, used for the measurements described in this paper, employing a commercial (Roper Scientific/Princeton Instruments "PI-Max") gated intensified CCD as the receiver. This detector technology, like the MCP/CDL, uses a micro-channel plate photomultiplier, but there the similarity ends. The CCD system has an ultimate time resolution of 2 ns, compared to 100 ps for the MCP/CDL, but this difference is unimportant for cloud measurements where relevant time scales are tens of ns and longer. More important are the differences in the basic modes of operation. Unlike the MCP/CDL system, which time-tags each photon individually, the gated CCD system achieves time resolution by electronically gating the intensifier, with gate width and gate delay relative to the laser pulse as adjustable parameters. The MCP/CDL system collects an entire time series for each laser pulse (although only a few photons per pulse can be collected), with good statistics achieved by integrating results over many pulses. The gated CCD, in contrast, collects many photons during its narrow time gate, at a specific delay after the laser pulse, again integrating multiple pulses to achieve good statistics, then it advances the gate delay to

10

collect the next movie "frame."

There are two main advantages of the gated CCD system. First, it can collect many more photons per laser pulse than the MCP/CDL system. Secondly, the adjustable gate width of the CCD system allows the exposure time to be adjusted automatically during the course of the measurement, with short exposures for the bright early returns, and longer exposures for the dim high-order scattering. This considerably ameliorates the problems caused by the large dynamic range of the cloud-scattered returns.

This time-domain strategy for dealing with the large dynamic range of typical cloud WAIL returns is an important improvement over our previous WAIL instrument. However, we continue to use our earlier, spatial-domain method to suppress the bright central peak associated with the initial laser impact on the cloud. This method uses the strong angular dependence of the wavelength passed by band-pass interference filters, which are used in any case to minimize contamination by background light. For a band-pass filter centered at a wavelength somewhat longer than the laser wavelength, the laser will be outside the pass band at normal incidence, but the filter's pass band will be shifted to the laser wavelength for a range of off-normal angles. Figure 2 illustrates this effect for our collection of 10 nm band-pass filters. To obtain unsaturated data with good signal-to-noise ratios for the entire angular range, we typically collect data using two or three filters with overlapping angular pass-bands, then splice the datasets to form a complete dataset covering the full angular range. Subsequent to the measurements described in this paper, we have found that this rather awkward splicing procedure can be avoided entirely by using a single filter with a wider bandpass that admits the full range of angles while still sufficiently reducing background light; the CCD's temporally-variable integration time alone can cope with the wide dynamic range.

We use a high-repetition-rate, low-energy-per-pulse laser, and average over many pulses

to attain good statistics, effectively making our system an imaging version of a micro-pulse lidar. Though the laser is used without any beam-expanding optics, the laser's intrinsic 3 mrad full-angle divergence spreads the beam sufficiently to become eye-safe at ranges greater than 1 km, significantly reducing the hazards to aircraft. The laser is a frequency-doubled Nd:YAG (Cutting Edge Optronics "Stilletto"), with a 30 ns pulse width, and pulse energy of approximately 0.5 mJ with a 4 kHz repetition rate is used here.

WAIL's CCD imager uses a 512×512 pixel array, but for the weakly variable cloud decks encountered here, such high spatial resolution is not required. Therefore, to keep data volumes more manageable, we use 4×4 on-chip binning to reduce the spatial sampling to an effective 128×128 pixels. The CCD camera is equipped with a commercial 12.5 mm focal length lens, resulting in a square FOV at the focal plane, 53.6° on a side ($\approx 0.42° \times 0.42°$ per pixel). The lens speed was set at $f/1.3$.

The FOV and angular mapping as a function of field position were directly measured in the laboratory, using targets placed at measured distances from the camera and at measured displacements from the camera's central axis. We find that lens's angular mapping onto the CCD image plane is nearly linear, with the angular width of an individual pixel varying by less than ten percent across the image, from 0.397° at the center of the image to 0.435° at the edges.

The spatial variation of the photometric response of the complete CCD/lens/filter system was calibrated in the laboratory for each interference filter, using a 30 cm diameter integrating sphere with a 10 cm aperture, illuminated with the 532 nm laser to produce a spatially-uniform calibration target. The camera lens was placed at the sphere aperture and full-frame images of this uniform target were obtained for each of the interference filters. After subtracting dark counts, the result is a set of 2-dimensional relative spatial response functions that are used to

correct all subsequent field data. This method takes into account not only the filter's angular response, but also lens vignetting and intrinsic variations in the CCD.

Figure 3 shows the two versions of WAIL in field deployments. The laser transmitter is the same for both cases; only the imaging system and associated lenses have changed. The movie-like nature of the WAIL datasets can be seen in Fig. 4, which shows four representative 2D "stills" from each of three WAIL "movies" — one for each of the three filters in Fig. 2. These data, obtained using the CCD version of WAIL deployed in Oklahoma, are part of the dataset analyzed further on. Each of the sequences shown in Fig. 4 begins with the impact of the laser pulse on the cloud bottom, followed by spreading of the light via multiple scattering within the cloud. The left-most sequence, obtained using the center-weighted (535 nm) filter (cf. Fig. 2), most closely approximates the qualitative behavior of the space-time Green function: spreading and dimming. The sequences on the right (540 nm and 546 nm) contain information from larger backscattering angles and illustrate two phenomena of interest. First, note how the early-time, on-beam signal is strong enough to be visible despite these filters' orders-of-magnitude normal incidence attenuation of the 532 nm laser wavelength (cf. Fig. 2). Second, note how at later times the photons escaping the cloud base at large distances from the beam eventually populate the angular annulus of admittance for these off-beam filters.

eam Lidar i nal odelin ith i usion

In order to interpret the WAIL data described above and extract physical information about the probed cloud, we need a realistic theory for the off-beam lidar signal. For this, we will invoke photon diffusion theory. In this section, we summarize the diffusion-based forward model the off-beam lidar signal used further on to infer geometrical cloud thickness and volume-averaged

extinction, hence mean optical depth.

e nitions and assumptions

The schematic in Fig. 1 shows the geometry of ground-based off-beam lidar observation. In the case of a simple conservatively scattering homogeneous "slab" cloud, the basic quantities are: geometrical thickness (H) and extinction coefficient (σ). In diffusion theory, the only characteristic of the phase function which matters is the mean cosine (g) of the scattering angle. To fully characterize our cloud sounding scheme we also need the distance between the lidar and the illuminated cloud boundary (d_{obs}). Table 1 summarizes these definitions, gives derived quantities, and provides some typical ranges.

The cloud homogeneity assumption used here is of course questionable. Although we are confident it did not cause much damage here, it is high priority to develop diffusion-based models with both vertical and horizontal variability parameters. Our previous exercises in moment-based/time-only retrievals using ground-based [Love et al., 2001] and space-based [Davis et al., 2001] off-beam signals established that the primary concern is vertical stratification of extinction in clouds driven by lift, radiation and microphysical processes. As for the horizontal variability driven by turbulence, Davis et al. [1997a] found an $\approx 10\%$ effect in their early numerical simulations of laser-beam propagation in fractal cloud models, a bias captured accurately by the analytical approach used by Davis et al. [2002] for transmission statistics. This is for the observables (low-order moments) in (1)–(2); the retrieved cloud properties H and τ are affected at the same level or less. The reason for this is that, being fractal in nature, horizontal fluctuations in optical depth have long-range correlations (several tens of km) and we are only interested in variance over a scale on the order of $\sqrt{\langle r^2 \rangle}$ in (2), a km or so at most (using the mean τ in the formula).

14

iffusion theoretical model and boundary layer orrections

To describe the WAIL signal, we use the diffusion framework [Ishimaru, 1978] and follow Polonsky and Davis [2004] closely but not exactly. Accordingly, we assume that boundary radiance, $I(t, \vec{r}, \mathbf{n})$, in the direction $\mathbf{n}$ (measured in coordinates (θ, ϕ) where θ is measured away the vertical z-axis) at position $\vec{r}$ (a 2D vector) and time t (after the pulse hits the lower cloud boundary) can be written

$$I(t, \vec{r}, \mathbf{n}) = G(t, \vec{r})u(\mathbf{n}) \tag{5}$$

where $G(t, \vec{r})$ is the reflective boundary Green function for a collimated source beam (normal to the boundary) and the angular distribution of reflected radiance is factored into $u(\mathbf{n})$. Letting c denote the speed of light, diffusion theory delivers our new lidar equation in closed-form as

$$G(t, \vec{r}) = \frac{\pi}{t(H + 2\chi)^2} \exp\left[-\frac{\vec{r}^2}{2\chi ct}\right] \sum_{m=1}^{\infty} m \sin\left(\frac{5\pi\chi m/2}{H + 2\chi}\right) \exp\left[-\frac{\chi ct}{2}\left(\frac{\pi m}{H + 2\chi}\right)^2\right] \tag{6}$$

where we adopt the classic [Eddington, 1916] expression for the "extrapolation" length

$$\chi = \frac{2/3}{(1 - g)\sigma} \tag{7}$$

(slightly different numerator values have been proposed), and

$$u(\mathbf{n}) = \frac{1}{4\pi}\left(1 + \frac{3}{2}\cos\theta\right). \tag{8}$$

We recognize here $1/(1-g)\sigma$ as the "transport" or "rescaled" mean-free-path of the photons.

Integration of (5) over t yields the steady-state version of the diffusion solution:

$$I(\vec{r}, \mathbf{n}) = G(\vec{r})u(\mathbf{n}), \tag{9}$$

where (6) leads to

$$G(\vec{r}) = \frac{\pi}{(H + 2\chi)^2} \sum_{m=1}^{\infty} m \sin\left(\frac{5\pi\chi m/2}{H + 2\chi}\right) K_0\left(\frac{\pi m\, r}{H + 2\chi}\right), \tag{10}$$

K_0 being the 0th-order modified Bessel function.

The main differences between the above expressions for the off-beam lidar signals and the counterparts for the space-time and space-only Green functions given by Polonsky and Davis [2004] is that (1) they were not concerned with the flux-to-radiance conversion term $u(\mathbf{n})$ and (2) they addressed the problem of embedded isotropic point-sources. Rather than integrating the point-source Green function over the appropriate exponential distribution, we start with a simpler asymptotic-theoretical expression for the collimated beam problem. Minor differences arise in the m-dependence of the coefficients of the exponential and Bessel-function terms in the summations. Has was the case for Polonsky and Davis [2004], one needs to invoke the Poisson sum-rule to convert the slowly converging series obtained by time integration of (6) into the above rapidly converging series in (10). For a full derivation, we refer to Polonsky and Davis [2005].

What is the accuracy of the above diffusion-based expressions? A priori, we trust (6), (7) and (10) but not (8) because diffusion is known to lose accuracy in the angular domain at the cloud boundaries.

To make this assessment, we performed Monte Carlo simulations for a homogeneous cloud with a [Deirmendjian, 1969] Cloud C.1 phase function and a geometrical thickness of 0.7 km at a range of 0.5 km. A forward Monte-Carlo scheme using 10^9 trajectories was used. The laser source generates a δ-pulse with unit energy so time dependencies of the boundary flux $G(t, \vec{r})$ at selected radial distances were obtained by Monte Carlo simulation and with (6) and (7). Results are plotted in Fig. 5, showing that diffusion accurately describes the time-dependence starting at an instant dependent on the radial distance. Similarly, we plot results for $G(\vec{r}) \equiv G(r)$ as a function of radial distance for the steady-state case. For the diffusion approximation in (10), results were multiplied by the factor of 0.83 to emphasize the similarity.

The need for this kind of adjustment is traceable [Davis et al., 1999, Polonsky and Davis, 2004] to the choice of 2/3 as numerator in (7) for χ, a boundary condition parameter in diffusion theory. This quantity indeed appears in all the sin functions used in the expansion (10).

Finally, we need to examine the accuracy of (5) with (8) for the angular dependence of the radiance. Given (5), the azimuthally-integrated lidar signal $F(t,\theta)$ is

$$F(t,\theta) = 2\pi \left(\frac{\cos\theta}{d_{\text{obs}}} \right)^2 G(t, r = d_{\text{obs}}\tan\theta)u(\cos\theta), \tag{11}$$

and we will denote its time-integral by $F(\theta)$. This provides us with a simple way to check the parameterization by comparing $u(\cos\theta)$ in (8) with the ratio

$$R(t,\theta) = \left(\frac{\cos\theta}{d_{\text{obs}}} \right)^2 \frac{F(t,\theta)/2\pi}{G(t, d_{\text{obs}}\tan\theta)} \tag{12}$$

for selected instants in time, using Monte Carlo to estimate the numerator. Results are displayed in Fig. 7. As expected, we see that $R(t,\theta)$ is substantially different from $u(\cos\theta)$ only at small ct and approaches the diffusion prediction at large enough ct, i.e., in asymptotic regime where we make our retrievals. For the steady-state solution, we compute the ratio

$$R(\theta) = \left(\frac{\cos\theta}{d_{\text{obs}}} \right)^2 \frac{\int_0^\infty F(t,\theta)\mathrm{d}t/2\pi}{\int_0^\infty G(t, d_{\text{obs}}\tan\theta)\mathrm{d}t} = \left(\frac{\cos\theta}{d_{\text{obs}}} \right)^2 \frac{F(\theta)/2\pi}{G(d_{\text{obs}}\tan\theta)}. \tag{13}$$

Results for several cloud optical thicknesses and lidar-cloud distances are plotted in Fig. 8, showing deviations of $R(\theta)$ from the literal prediction of the diffusion approximation in (8) that need to be corrected. This is basically WAIL's radiance-to-flux conversion and the empirical function

$$u_{\text{emp}}(\theta) = \text{const} \times \exp(5.6\cos\theta) \tag{14}$$

shown by the dashed lines provides a reasonable approximation independently of cloud parameters (since the multiplicative constant absorbs the overall reflectance value dependent on τ). We will use this empirical relation to estimate flux $G[\theta = \arctan(r/d_{\text{obs}})]$ at the cloud boundary from the observed lidar signal $F(\theta)$ in the steady-state case.

17

he ar h   A   ite eployment

The data described and analyzed here was obtained at one of the U.S. Department of Energy (DOE) ARM program's Cloud and Radiation Testbed (CART) sites. Specifically, WAIL was deployed at the SGP site in north-central Oklahoma simultaneously with over-flights by NASA's THOR instrument. Cahalan et al. [2004] gives a comprehensive overview of the synoptic situation. The data analyzed here were collected between 7:30 and 8:00 UTC when cloud base was at its maximum height during the observation period. This gives us the widest possible sampling of the off-beam signal distribution, although it is still quite severely truncated compared to previous deployments [Love et al., 2001; 2002].

As discussed above, both angular and temporal strategies for mitigating the large dynamic range were used. Each complete dataset consists of three pieces obtained sequentially: a dataset using an interference filter nominally centered at 535 nm, showing scattering in the central region near the initial laser impact on the cloud; another obtained with a 540 nm filter emphasizing intermediate viewing angles (roughly between $10°$ and $20°$); and a third obtained using a 546 nm filter for the largest viewing angles. Each dataset consists of 301 frames, having gate delays ranging from 0.70 μs to 15.70 μs after the laser pulse, with a constant gate delay increment of 50 ns. For each of these datasets, the CCD gate width was increased linearly with time, ranging from 5 ns to 100 ns for the small scattering angle data, and from 50 ns to 250 ns for the two wider-angle datasets. Eventually the integration time becomes longer than the delay increment for the latter part of each dataset. The 50 ns increment refers to the beginning of each integration period. Thus, for later frames, the integration periods for adjacent frames overlap. This has little effect on the end result because the multiple scattering decay is slowly varying at long times. The frame-number-dependent integration time is accounted for in the analysis. Two thousand laser shots are averaged for each frame

in order to obtain good statistics. Each dataset takes approximately 2.5 minutes to collect. The appropriate portions of the three spatially-overlapping datasets are then spliced together to form a complete dataset covering the full range of angles.

Table 2 shows the times at which the measurements were performed, along with other measurement characteristics. The complete set of measurements were collected during an interval of approximately 50 min. The raw outcome of a WAIL measurement is a 3-dimensional dataset which contains one temporal and two angular dimensions (cf. Fig. 4). We will see that the cloud field observed here had relatively high horizontal homogeneity, we therefore perform azimuthal averages resulting in substantial noise reduction. Only the dependencies on zenith angle and on time will be further analyzed.

A L ata A nalysis

Figure 9 shows the time dependence of the WAIL signal detected by the central pixel with the 535 nm filter at 7:23, 7:52 and 7:59 UTC. These signals coincide well, demonstrating a high degree of horizontal homogeneity of the lower part of the cloud during the whole observation period. This statement about horizontal homogeneity is confirmed by mm-radar reflectivity profiles in Fig. 14 and that dataset shows that it can be extended to the vertical direction for our two separate 3-filter collects starting respectively at 7:28 and 7:59 UTC.

At present the theory assumes a uniform cloud which seems to be justified for the two periods of interest identified in Table 2. This assumption guides the execution of our first task which is to determine cloud-base height. The lidar signal reflected from a homogeneous slab contains a very sharp increase coinciding with the cloud's lower boundary. Accordingly, the on-beam WAIL signal in Fig. 9 shows that cloud base is at a range of about 0.5 km.

We start with time-integrated off-beam signals, the steady-state or "cw" distribution of the reflected radiance in (10). The empirical function in (14) is used to convert the measured signal to the flux density distribution predicted by theory. Since the average cosine of the scattering angle for water-droplet clouds is ≈ 0.85 [Deirmendjian, 1969, Gerber, 2000], we have only two uniform slab-cloud parameters to estimate: geometrical thickness H and extinction coefficient σ which, by multiplication, give optical thickness τ. This is done by forming a standard "observed-predicted" cost function, computed over relevant range of $r = d_{\mathrm{obs}} \tan \theta$, that is minimized by varying the two cloud parameters. Consistent with our homogeneity assumption, we average the WAIL signal azimuthally, resulting in substantial measurement error decrease. The trivial normalization parameter in (14) is also estimated through the fitting procedure to account for the present lack of absolute calibration in WAIL. The upper panel of Fig. 10 shows the cost function for the relevant range of $\{H, \sigma\}$ using the WAIL signal measured at 7:30 UTC with $10° \leq \theta \leq 26°$. The mostly vertical orientation of the isolines clearly shows that the time-integrated signal helps mostly to determine σ.

The same analysis is repeated for the time-resolved data and displayed in the lower panel of Fig. 10). It shows isolines with mostly horizontal orientation and, thus, time-resolved data enables estimation of H. In this case, we used the diffusion prediction in (6), 7:30 UTC WAIL data for $\theta = 26.6^c irc$ and range (i.e., $ct/2 + d_{\mathrm{obs}}/\cos\theta$) between 1.0 and 1.9 km. Although our data is too truncated to estimate them, moments are consistent with these findings. Time-dependence is dominated by H since τ only enters through correction terms for (1) and in higher-order moments such as (4). By the same token, variance of the horizontal transport, i.e., $\langle r^2 \rangle$ from (2), goes as H/σ, so extinction changes have a first-order effect.

We can combine the advantages of both the time-resolved and time- integrated data analyses by constructing a weighted sum of the cost functions, each one being normalized naturally

20

by its minimum. In this case, the ratio is about 4:1 in favor of the time-integrated data because of its reduced noise level. The result is in Fig. 11 (upper panel), showing a clear minimum at $H = 0.45$ km and $\sigma = 48$ km^{-1}. An objective analysis using nonlinear regression yields an uncertainty on σ of 3 km^{-1} and 0.09 km for H. Figure 11 (lower panel) repeats this for WAIL signals detected at 8:00 UTC, yielding $H = 0.6 \pm 0.2$ km and $\sigma = 50.5 \pm 3$ km^{-1}. The corresponding optical thickness estimates are 21.6 ± 5.7 at 7:30 UTC and 30.3 ± 11.8 at 8:00 UTC. The large uncertainties in the geometrical thickness and optical thickness, especially at 8:00 UTC, are traceable directly to the insufficient FOV for the low cloud ceiling (combined with relatively large cloud thickness). We discuss further on a simple remedy for this situation without modifying WAIL's present specifications. To conclude the discussion of our retrieval technique, we demonstrate in Fig. 12 how the adjusted diffusion theory predictions compare with the signals measured at 7:30 UTC. Note that the arrowed lines show the independent-variable ranges over which the parameter fit has performed.

Comparison ith A nstruments

Our WAIL measurements described and analyzed above were performed at the ARM Climate Research Facility (ACRF) in Oklahoma, where cloud observations are made routinely. ARM cloud instruments used here are the laser ceilometer, micro-pulse lidar, microwave radiometer, and millimeter-wavelength cloud radar. We now compare their determinations with WAIL's.

Laser eilometer and mi ro pulse lidar

The Vaisala Ceilometer (VCL) is a single-purpose lidar operating in near infrared (905 nm). Ceilometer cloud-base heights of interest are depicted in Fig. 13. The micro-pulse lidar (MPL)

delvers both cloud-base and -top heights, operating at 523.5 nm (very close to WAIL's 532 nm wavelength). Cloud boundary heights from the MPL are in Fig. 13: base and top heights are in dashed and dash-dotted lines respectively. MPL's estimation of geometrical thickness of the cloud is 0.1-0.2 km. Of course the MPL's cloud-top product is biased very low in the case of this optically thick cloud layer since it is assumed (1) that multiple scattering does not contaminate significantly the directly transmitted beam and (2) that it can reach cloud top on a two-way trip through the cloud. Neither of these conditions is satisfied here, so we will not discuss MPL cloud tops any further.

Our two (on-beam) inferences of mean cloud base in Fig. 13 are at 0.5 km; they agree with the VCL (at most 50 m higher) but the MPL estimate are up to 100 m lower. Although we have not examined the MPL algorithm in any detail, we attribute this systematic discrepancy between ARM instruments with the fact that extinction coefficient profiles in clouds are generally represented as increasing more-or-less rapidly from the zero level. In this case the maximum of the (on-beam) lidar signal does not coincide with the cloud-base (i.e., vanishing extinction) level and this necessarily complicates cloud base detection. If we adopt the MPL definition of cloud base as a way of anticipating how a vertically-varying model for cloud extinction would behave, then we can adjust our estimates of cloud thickness to $\approx$0.55 at 7:30 UTC and $\approx$0.7 km at 8:00. This correction would not affect cloud optical thickness estimates.

illimeter ave loud radar and H

The mm-wave cloud radar (MMCR) probes internal cloud structure and detects boundaries. The two-dimensional chart of the reflectivity in Fig. 14 characterizes the cloud's inner and outer structure during our deployment. We also plot the position of the cloud layer according to WAIL which, accounting for our uncertainties, is close to what the MMCR sees. There

is no other nearby ARM instrument providing cloud-top height. There is however a THOR cloud-top estimate of 1.07 km at 7:18 UTC (THOR was then between 0.3 and 1 km away from the SGP central facility, measured horizontally) which is consistent with the MMCR reading.

For reference, Fig. 13 shows the ±0.1 km variability of cloud-top height according to the airborne THOR lidar during our observation period. The NASA P-3 was then too far from the central facility for direct comparison with WAIL. However, we note that the cloud tops from the WAIL and THOR instruments track each other, within the variability and uncertainty.

Figures 13–14 show that our two *mean* cloud top estimates are, if anything, 50-100 m lower than the corresponding means of the *fluctuating* MMCR and THOR counterparts. Targeting cloud thickness H, this small bias at cloud top is in addition to the one already identified at cloud base of similar magnitude. This time however, it cannot be attributed to the vertical homogeneity assumption [Love et al., 2001] but rather to the truncation problem. We therefore expect this bias to diminish along with the overall uncertainty as WAIL's FOV is widened.

i ro ave radiometer

The microwave radiometer (MWR) measures column-integrated amounts of water vapor and (cloud) liquid water. Using this data we can estimate cloud optical thickness [Stephens, 1978]:

$$\tau_H = \frac{3}{2}\frac{\text{LWP}}{r_{\text{e}}}, \tag{15}$$

where LWP is the liquid water path measured by MWR in cm (or mm), and r_{e} is the effective radius of the cloud particles in the same units. It is commonly assumed that $r_{\text{e}} \approx 10~\mu\text{m} = 10^{-3}$ cm. This estimation of optical thickness is shown in Fig. 15 vis-'-vis LWP in cm.

Being a vertical integral through all the 3D variability that plagues all cloud boundary retrievals, optical depth estimation and comparison should be easier, but maybe not. We

estimate cloud optical thickness at ≈ 21.6 for the 7:30 UTC collect and ≈ 30.3 at 8:00 UTC, consistently $\approx 20\%$ over the MWR values. This suggests that r_e may have been that much less than the canonical 10 μm value used in the LWP-to-τ conversion.

is ussion

The above analysis of agreement and disagreement between various cloud probing devices notwithstanding, it is important to bear in mind that the very definition of a real cloud's boundary will —and should— depend on the particulars of the instrument (wavelength, FOV, space-time sampling and averaging, etc.) as well as on the conceptual picture that the algorithm developer had in mind. Under these conditions, the tracking we get between different instruments (and even more so with the THOR instrument) is tantamount to a successful validation of the off-beam lidar technique, if not the WAIL instrument itself (more observations are needed under a wider variety of conditions).

Inasmuch as we see real disagreement between instruments, the next logical question is of course which instrument are we going to believe? In our view, the answer should come from the application in mind which is rarely some fundamental "truth" about the properties of some designated cloud. As an example, and without comprehensive analysis of all possible methods, the MWR may be the best source for LWP if the hydrological cycle is the focus. In contrast, if climate and radiation are at the scientific focus, then optical depth from WAIL may be a more judicious choice since it operates at an energetically relevant wavelength and, in sharp contrast with the MWR, no assumptions about cloud microphysics are required.

ummary and utloo

We analyzed WAIL data collected during a field campaign where several radically different cloud instruments were operating. Comparison of the results shows that even the simplest possible modeling assumption, that the cloud is a homogeneous slab, yields very reasonable estimates of the cloud's geometrical characteristics: base height and geometrical thickness, hence cloud-top height. Our estimates of cloud optical thickness also coincide well with the available data. Only two values of the geometrical and optical thicknesses were obtained, one each at the beginning and end of a relatively short interval when the cloud ceiling was at its maximum of ≈ 0.5 km during the deployment. At other times, cloud base was so low that (in spite of a $57°$ full-width FOV) the off-beam signal was too severely truncated to even attempt cloud property retrievals. The homogeneous cloud model used here is determined only by its geometrical and optical thicknesses and can already reproduce accurately the observed space-time cloud reflectance characteristics for large-enough times and distances. In this sense, the uniform model can be viewed as an optical equivalent to the real 3D cloud being probed.

Our future research will be to develop appropriate procedures to retrieve cloud structure with more fidelity by means of more complete use of WAIL's capabilities. The logical starting point is to retrieve the extinction coefficient profile and then a volume-averaged measure of the horizontal variability. We have obtained preliminary results on both accounts in the forward modeling without leaving the productive framework of diffusion theory. Additionally, presently untapped portions of WAIL signals are to small-angle multiple scattering modeling. This enhancement will enable more accurate determination of cloud parameters near the irradiated boundary, specifically, extinction profile (leading to better cloud bases) and effective droplet radius.

Overall, the limited validation we obtained of the WAIL instrument based on a single case

study at the ARM site is a significant milestone because there is a relatively easy way of overcoming the truncation problem that restricted the amount of useful data. This problem occurs only in ground-based configurations when the cloud base is low and is mitigated simply by using a shorter focal length lens (the current lens corresponds to a moderately wide-angle photographic lens). The angular truncation problem can be further ameliorated by tilting the receiver so that the image of the impact point of the beam on cloud base is moved from the center to a corner of the focal plane, which more than doubles the range of angles relative to the beam. This solution is possible because of the unique advantage of having an imaging device at the focal plane of the receiver. For the present fore-optics, we would be going from $\theta_{\max} = 26.8°$ to $\theta_{\max} \gtrsim 55°$ thus, for a cloud base at 0.5 km, we would go from a maximum off-beam distance of 0.25 km to 0.87 km or better. The minor cost of this modification is a $\approx 90°$ sample in azimuth (down from 360°) from a few degrees up to $\approx 60°$ from zenith (using the present lens), and somewhat less at larger zenith angles. With this flexible spatial/angular sampling, we know from asymptotic diffusion theory [Polonsky and Davis, 2004] that moment-based methods and single-term expansions for the response become accurate. Far simpler data analysis methods than used here thus become available. Even in a thick fog scenario where cloud base is at ground level, the beam can be removed completely from the receiver's FOV; WAIL thus becomes an "in-situ" cloud lidar and the time-domain techniques proposed by Evans [2003] apply. Another procedural simplification follows from using a single but wider-band background-suppression filter. The cost in increased background noise can easily be offset by a slightly longer exposure (now at 2.5 min).

The most exciting instrumental development by far will be successful demonstration of filters narrow enough for daytime operation. We have already achieved a good signal-to-noise ratio under the full moon, which is $\approx 10^6$ times dimmer than daylight. A factor of $\approx 10^6$

improvement in background rejection is needed to maintain a comparable signal-to-noise level in full daylight. A rudimentary approach for realizing some coarsely-sampled off-beam lidar results in daylight derives from the method of automatic background tracking and subtraction used for the very first detection of diffusing lidar photons [Davis et al., 1999]. This early success was accomplished simply by deflecting the transmitter's beam away from the narrow ($\approx$1 mrad) field-of-view of an otherwise quite standard zenith-pointing lidar system ($\approx$0.5 J pulses at 1064 nm, 10 Hz rep-rate, 40 cm aperture). The off-beam signal was easily detected above the background noise out to $12°$ away from zenith in broad daylight. We are presently pursuing a solution based on an ultra-narrow ($\approx$0.005 nm) magneto-optic filter design that operates on one of the sodium doublet lines near 589 nm. The combination of narrow filter bandwidth with the existence of a strong sodium Fraunhofer absorption at precisely the same wavelength brings us close to our background-rejection goal. We refer the reader to Love et al. [2002] for a recent progress report on this strategy, which calls for a tunable laser source locked at the filter-selected wavelength.

In summary, the joint WAIL and THOR campaign conducted at the ARM Southern Great Plains CART site confirmed the validity of off-beam lidar as a worthy concept in cloud remote sensing. In spite of an inconveniently low cloud base resulting in a spatially-truncated photon distribution data from the ground-based WAIL, success was achieved by employing the diffusion theory of Polonsky and Davis [2004] that predicts the distribution and not just its moments. The off-beam lidar retrievals of cloud characteristics agreed well, within the established uncertainty, with independent observations of the cloud parameters. We are looking forward to seeing widespread use of off-beam (multiple-scattering) lidar techniques not only for terrestrial clouds, but also for vegetation canopies [Kotchenova et al., 2003], ice, snow, and so on. Eventually, as more compact and powerful laser sources become available, observations

from spacecraft will become a option. This opens up applications in planetary science, such as sounding Europa's icy surface which is thought by some at least to be relatively thin.

eferen es

Bissonnette, L.R., 1996: Multiple-scattering lidar equation. *Appl. Opt.*, vol.35, pp. 6449–6465.

Bissonnette, L.R., G. Roy, L. Poutier, S.G. Cober, and G.A. Isaac, 2002: Multiple-scattering lidar retrieval method: Tests on Monte Carlo simulations and comparisons with in situ measurements. *Appl. Opt.*, vol. 41, pp. 6307–6324.

Cahalan, R.F., and J.B. Snider, 1989: Marine stratocumulus structure during FIRE. *Remote Sens. Environ.*, vol. 28, pp. 95–107.

Cahalan, R.F., M. J. McGill, J. Kolasinski, T. Varnai, and K. Yetzer, 2004: THOR, cloud THickness from Offbeam lidar Returns. *J. Atmos. and Oceanic Tech.*, this volume.

Clothiaux, E.E., M.A. Miller, B.A. Albrecht, T.P. Ackerman, J. Verlinde, D.M. Babb, R.M. Peters, and W.J. Syrett, 1995: An evaluation of a 94-GHz radar for remote sensing of cloud properties, *J. Atmos. and Oceanic Technol.*, vol. 12, pp. 201–229.

Davis, A., A. Marshak, R.F. Cahalan, and W.J. Wiscombe, 1997a: The LANDSAT scale-break in stratocumulus as a three-dimensional radiative transfer effect, Implications for cloud remote sensing, *J. Atmos. Sci.*, vol. 54, pp. 241–260.

Davis, A., D.M. Winker, A. Marshak, J.D. Spinhirne, R.F. Cahalan, S. Love, S.H. Melfi, and W.J. Wiscombe, 1997b: Retrieval of physical and optical cloud thicknesses from space-borne and wide-angle lidar, In *Advances in Atmospheric Remote Sensing with Lidar.*, A. Ansmann, R, Neuber, P. Rairoux, and U. Wadinger, editors, Springer-Verlag, Heidelberg (DGR), pp. 193–196.

Davis, A.B., C. Ho, and S.P. Love, 1998: Off-beam (multiply-scattered) lidar returns from stratus, 2: Space-time measurements in a laboratory simulation. In *19th International Laser*

Radar Conference Proceedings, Annapolis (Md), July 6-10, 1998, U. Singh, S. Ismail, and G. Schwemmer, editors, NASA Center for Aero-Space Information (CASI), pp. 55–58.

Davis, A.B., 1999: Physical thickness and optical depth of stratocumulus from space-borne lidar, A moment-based diffusion method. In *Technical Digest of OSA Topical Meeting "Optical Remote Sensing of the Atmosphere"*, June 21-25, Santa Barbara (Ca), Optical Society of America, Washington (DC), pp. 66–68.

Davis, A.B., R.F. Cahalan, J. D. Spinhirne, M.J. McGill, and S.P. Love, 1999: Off-beam lidar: An emerging technique in cloud remote sensing based on radiative Green-function theory in the diffusion domain. *Phys. Chem. Earth (B)*, vol. 24, pp. 757–765.

Davis, A.B., D.M. Winker, and M.A. Vaughan, 2001: First retrievals of dense cloud properties from off-Beam/Multiple-scattering lidar data collected in space. In *Laser Remote Sensing of the Atmosphere: Selected Papers from the 20th International Conference on Laser Radar*, A. Dabas and J. Pelon, editors, Ecole Polytechnique, Palaiseau (France), pp. 35–38.

Davis, A.B., and A. Marshak, 2002: Space-time characteristics of light transmitted by dense clouds, a Green function analysis, *J. Atmos. Sci.*, vol. 59, pp. 2713–2727.

Deirmendjian, D., 1969: *Electromagnetic Scattering on Spherical Polydispersions.* Elsevier Publ. Co., New York (NY).

Eddington, A.S., 1916: On the radiative equilibrium of stars, *Mon. Not. Roy. Ast. Soc.*, vol. 77, pp. 16–35.

Einstein, A., 1905: On the motion, required by the molecular-kinetic theory of heat, of particles suspended in a fluid at rest, *Ann. Phys.* (Leipzig), vol. 17, pp. 549–560.

Evans, K.F., R.P. Lawson, P. Zmarzly, D.O'Connor, and W.J. Wiscombe, 2003: In situ cloud sensing with multiple scattering lidar: Simulations and demonstration. *J. Atmos. and Oceanic Tech.*, vol. 20, pp. 1505–1522.

Gerber, H., Y. Takano, T.J. Garrett, and P.V. Hobbs, 2000: Nephelometer measurements of the asymmetry parameter, volume extinction coefficient, and backscatter ratio in Arctic clouds. *J. Atmos. Sci.*, vol. 57, pp. 3021–3034

Ishimaru, A., 1978: *Wave Propagation and Scattering in Random Media.* Academic Press, New York (NY).

King, M.D., 1986: Multiwavelength scanning radiometer from airborne measurements of scattered radiation within clouds. *J. Atmos. and Oceanic Technol.*, 3, 513–522.

King, M.D., L.F. Radke, and P.V. Hobbs, 1990: Determination of the spectral absorption of solar radiation by marine stratocumulus clouds from airborne measurements within clouds. *J. Atmos. Sci.*, vol. 47, pp. 894–907.

Kotchenova, S.Y., N.V. Shabanov, Y. Knyazikhin, A.B. Davis, R. Dubayah, and R.B. Myneni, 2003: Modeling lidar waveforms with time-dependent stochastic radiative transfer theory for remote estimations of forest biomass, *J. Geophys. Res.*, vol. 108, pp. 4484–4496.

Liljegren, J.C., 1994: Two-channel microwave radiometer for observations of total column precipitable water vapor and cloud liquid water path. In *Fifth AMS Symposium on Global Change Studies*, Nashville (Tn), January 23-28, 1994, Am. Meteor. Soc., Boston (Ma), pp. 262–269.

Lonnqvist, J., 1995: Experiences with a novel single-lens cloud height lidar. In *Ninth*

AMS Symposium on Meteorological Observations and Instrumentation, Boston (Ma), 27-31 March, 1995, Am. Meteor. Soc., Boston (Ma), pp. 106–109.

Love, S.P., A.B. Davis, C.A. Rohde, and C. Ho, 2001: Remote sensing of cloud thickness and liquid water content with wide-angle imaging lidar. *Atm. Res.*, vol. 59, pp. 295–312.

Love, S.P., A.B. Davis, C.A. Rohde, L. Tellier, and C. Ho, 2002: Active probing of cloud multiple scattering, optical depth, vertical thickness, and liquid water content using wide-angle imaging lidar. In "Atmospheric Radiation Measurements and Applications in Climate," J. A. Shaw, editor, *SPIE Proceedings*, vol. 4815, pp. 129–138.

Marshak, A., A. Davis, W.J. Wiscombe, and R.F. Cahalan, 1995: Radiative smoothing in fractal clouds, *J. Geophys. Res.*, vol. 100, pp. 26,247–26,261.

Meador, W.E., and W.R. Weaver, 1980: Two-stream approximations to radiative transfer in planetary atmospheres: A unified description of existing methods and a new improvement, *J. Atmos. Sci.*, vol. 37, pp. 630–643.

Miller, S.D., and G.L. Stephens, 1999: Multiple scattering effects in the lidar pulse stretching problem, *J. Geophys. Res.*, vol. 104, pp. 22,205–22,219.

Min, Q.L., and L.C. Harrison, 1996: Cloud properties derived from surface MFRSR measurements and comparison with GOES results at the ARM SGP site. *Geophys. Res. Lett.*, vol. 23, pp. 1641–1644.

Moran, K.P., B.E. Martner, M.J. Post, R.A. Kropfli, and D.C. Welsh, 1998: An unattended cloud-profiling radar for use in climate research. *Bull. Amer. Meteor. Soc.*, vol. 79, pp. 443–455.

Nakajima, T.Y., and M.D. King, 1990: Determination of the optical thickness and effective particle radius of clouds from reflected solar radiation measurements - Part I, Theory, *J. Atmos. Sci.*, vol. 47, pp. 1878–1893.

Polonsky, I.N., and A.B. Davis, 2004: Lateral photon transport in dense scattering and weakly-absorbing media of finite thickness: Asymptotic analysis of the Green functions. *J. Opt. Soc. Amer. A*, vol. 21, pp. 1018–1025.

Polonsky, I.N., and A.B. Davis, 2005: Off-Beam Cloud Lidar: A New Diffusion Model and an Analysis of LITE Returns, Los Alamos National Laboratory Unclassified Report, LA-UR-04-XXXX, available from the authors.

Priedhorsky, W.C., R.C. Smith, and C. Ho, 1996: Laser ranging and mapping with a photon-counting detector. *Appl. Opt.*, vol. 35, pp. 441–452.

Schuster, A., 1905: Radiation through a foggy atmosphere, *Astrophys. J.*, vol. 21, pp. 1–22.

Spinhirne, J.D., 1993: Micro-pulse lidar. *IEEE Trans. Geosc. and Remote Sens.*, vol. 31, pp. 38–55.

Stephens, G.L., 1978: Radiation profiles in extended water clouds. II. Parameterization schemes *J. Atmos. Sci.*, vol. 35, pp. 2123–2132.

Zege, E.P., I.L. Katsev, and I.N. Polonsky, 1994: Analytical solution to LIDAR return signals from clouds with regard to multiple scattering. *Appl. Phys.*, vol. B58, pp. 345–353.

Table 1: Key variables and cloud parameters, with plausible ranges, in ground-based off-beam lidar.

Notation	Definition	Typical Range	Units
d_{obs}	lidar-cloud range[1]	$0.5 - \infty$	km
θ	observation zenith angle[2]	$0 - 30$	degrees
r	$d_{\mathrm{obs}} \tan\theta$, radial distance from beam	≥ 0	km
ct	photon path length inside the cloud	≥ 0	km
H	cloud geometrical thickness[3]	$0.3 - 3$	km
σ	extinction coefficient	$20 - 200$	km^{-1}
MFP	$1/\sigma$, photon mean free path	$5 - 50$	m
τ	$\sigma H = H/\mathrm{MFP}$, optical thickness[4]	$\gtrsim 6$	
β	scattering angle	$0 - 1 0$	degrees
g	$< \cos\beta >$, asymmetry factor	$\approx 0. 5$	

The "infinite" range case corresponds to space-based observation where r can be $\approx$1 km while θ is still within a few mrad. For a successful application of "off-beam" lidar techniques to LITE observations of a dense marine stratocumulus layer, see Davis et al. [2001].

Our present optics have $\theta \approx 27$ but by moving the beam impact point from the center to the corner of the the focal plane image, one can more than double θ; as described in the text, this is achieved by mechanically tilting the receiver mount while leaving the transmitted beam vertical.

The ability of off-beam lidar to detect more than one cloud layer has yet to be determined. So what we have in mind here is the maximum thickness of a single-layer cloud of the stratus type.

The minimum value assigned to τ for off-beam lidar corresponds to $(1 - g)\tau \approx 1$ (with $g \approx 0.85$) which is where diffusion theory becomes accurate. This also corresponds roughly to were on-beam lidar fails to achieve 2-way transmission.

Table 2: Timetable of measurements performed ith WA L on March 25, 2002. The laser o   is the modality used to measure the background noise. The designations   1 and   2 identify the 3 collects that   here merged into our 2 analysis datasets.

ilter nm	Time T C	Shots per time-bin	Time-bin idth ns	Comment
535	7:23	2000	5-100	
	7:2	2000	5-100	1
	7:52	2000	5-100	
	7:54	2000	5-100	laser o
	7:5	2000	5-100	2
540	7:32	2000	50-250	1
	:0	2000	50-250	2
	:14	2000	50-250	laser o
546	7:35	5000	50-250	1
	7:43	5000	50-250	laser o
	:02	5000	50-250	2
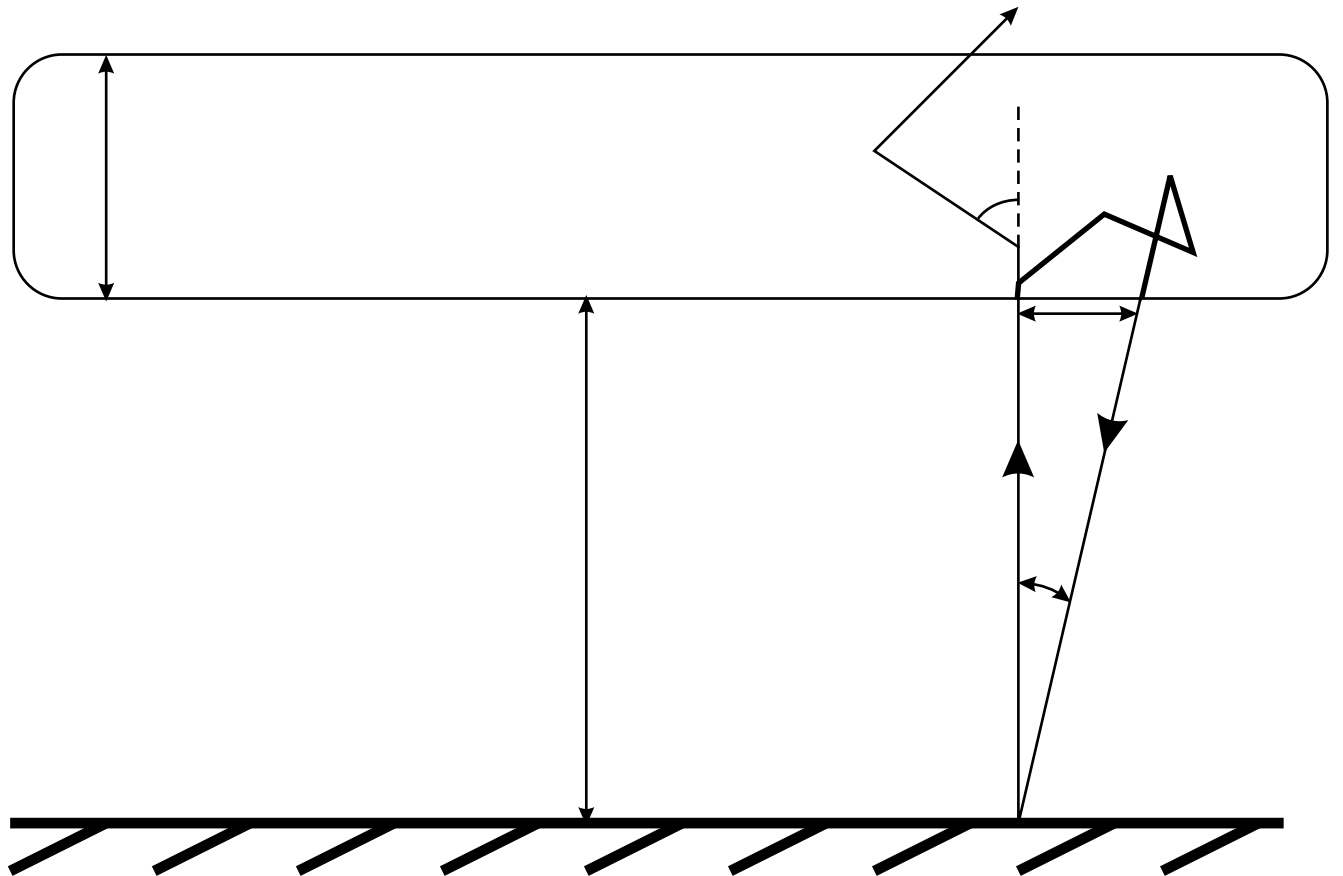
igure 1: Geometry of ground-based o -beam lidar obser ation. See Table 1 for de nitions and ranges for the ariables and parameters of the problem.
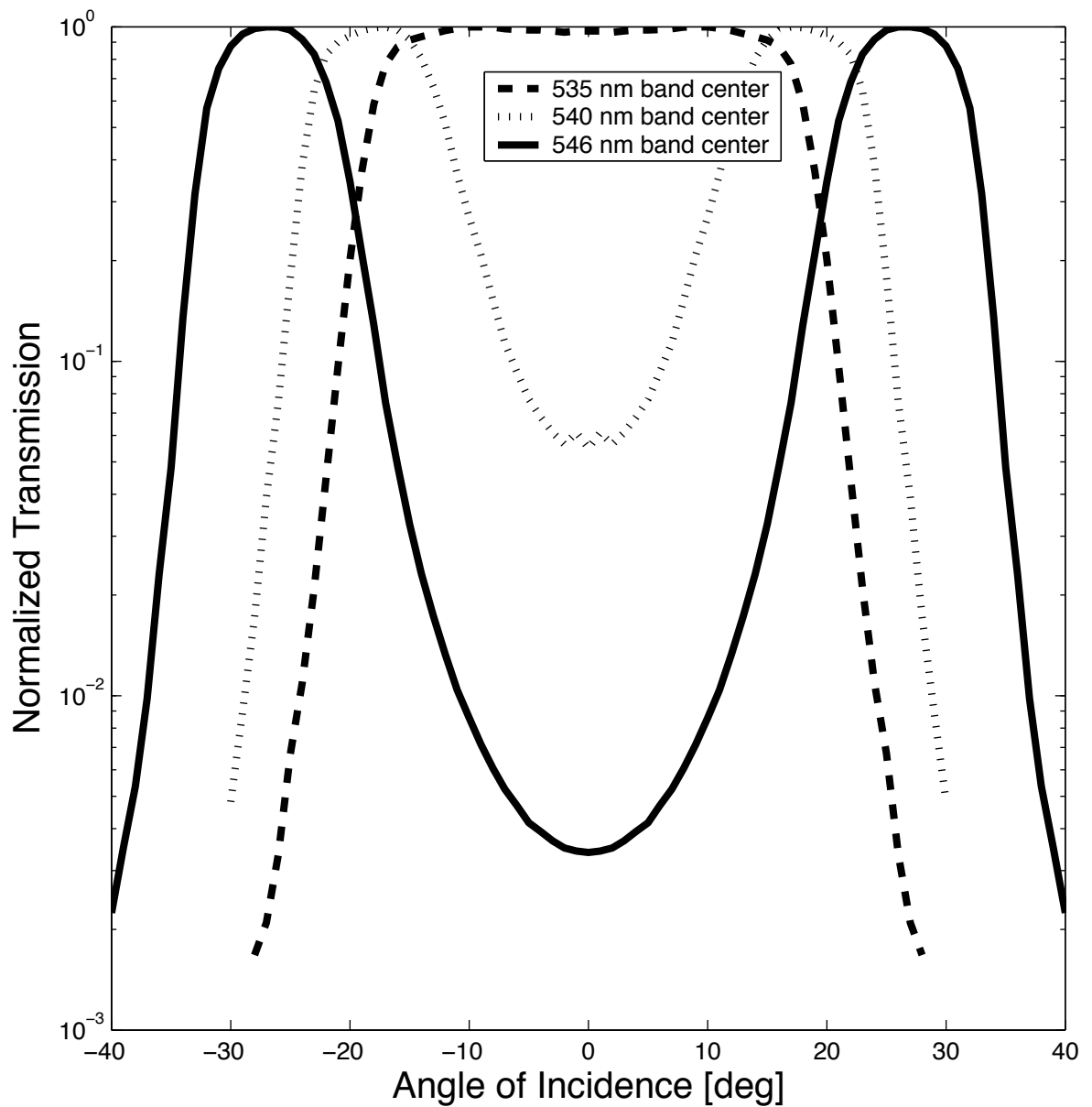
igure 2: Bandpass interference lters as angular response lters. Transmission at 532 nm as a function of angle of incidence for our 10-nm bandpass interference lter collection. The band centers listed in the gure refer to normal incidence. The lter s center a elength shifts to shorter a elengths for o -normal incidence, leading to a angularly- arying transmittance for a gi en ed a elength. This e ect is used to suppress the bright central spot of cloud WA L returns.

igure 3: T o incarnations of the WA L system for cloud obser ations: (a) The MCP/CDL ersion of WA L, deployed at enton Hill Obser atory, e Me ico, in A pril 1 (see Lo e et al. 2001 for results from this stand-alone WA L campaign). (b) The gated intensi ed CCD ersion, deployed at the A RM SGP site near Lamont, Oklahoma, in March 2002. The laser transmitter is the same for both ersions (see te t for details).
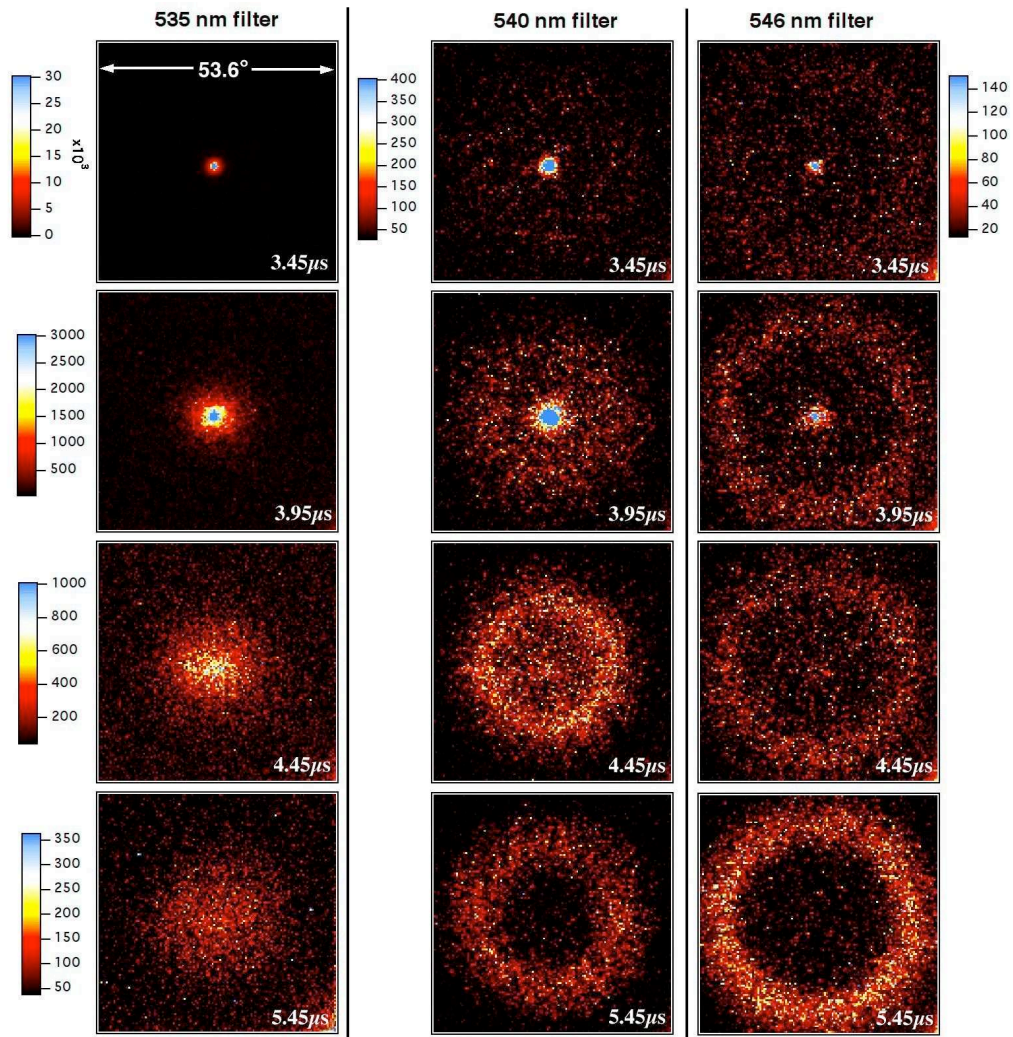
Figure 4: Sample frames from WAIL datasets obtained at the Oklahoma CART site between 7:23 and 7:35 UTC on March 25, 2002. Shown here are sequences obtained using three different background-suppression interference filters that optimize for different ranges of observation angle. The first (535 nm nominal band center) emphasizes the central, small-angle region, the second (540 nm) emphasizes the intermediate region, and the third (546 nm) emphasizes large angles (cf. Fig. 2)). Each frame has a 53.6° square FOV. The time delay after the laser pulse is noted on each frame. The color scales are adjusted as needed to visualize the image. In each sequence, one sees the initial impact of the laser pulse on the cloud, with subsequent decay and diffusive spreading of the light via multiple scattering. The annular appearance of the scattered distribution, seen at long times in the sequences for the 540 nm and 546 nm filters, is an artifact of those filters. The illuminated area seen in the bottom row illustrates the approximate useful range of angles for each filter.

45
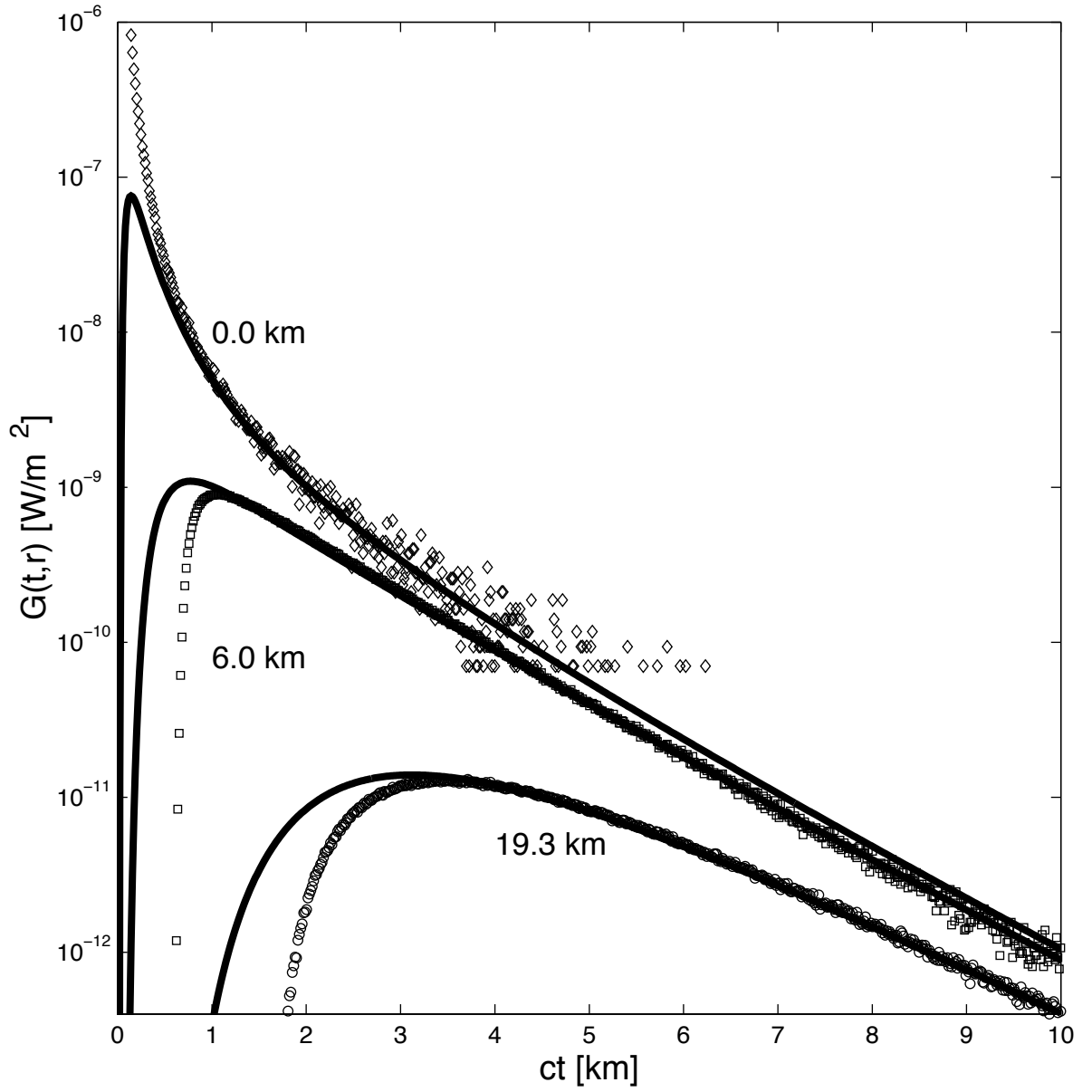
igure 5: Boundary u $G(t,r)$ as a function of ct for a 1 J pulse. Di usion appro imation predictions are sho n by solid black lines hile Monte Carlo results are depicted by the symbols. T he alues at the cur es are radial distance. Cloud geometrical thickness is 0.7 km and optical thickness is 25. T he phase function is highly for ard-peaked (D eirmend ian Cloud C.1).
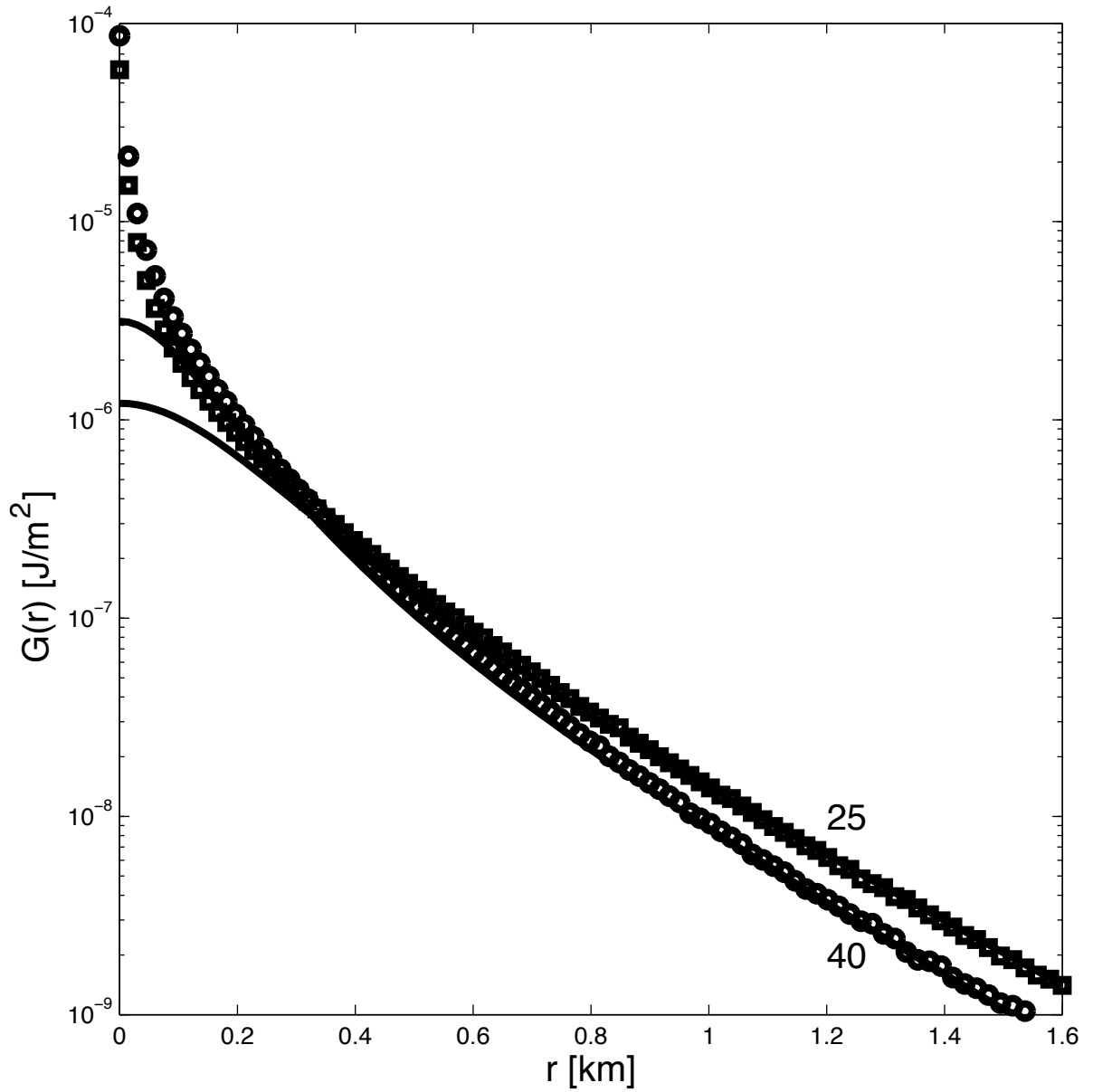
igure 6: Boundary u $G(r)$ as a function of r for a 1 J pulse. Di usion appro imation predictions are sho n by solid black lines hile Monte Carlo results are depicted by symbols. The alues at the cur es are cloud optical thickness. Cloud geometrical thickness is 0.7 km and the scattering phase function is Deirmend ian Cloud C.1.
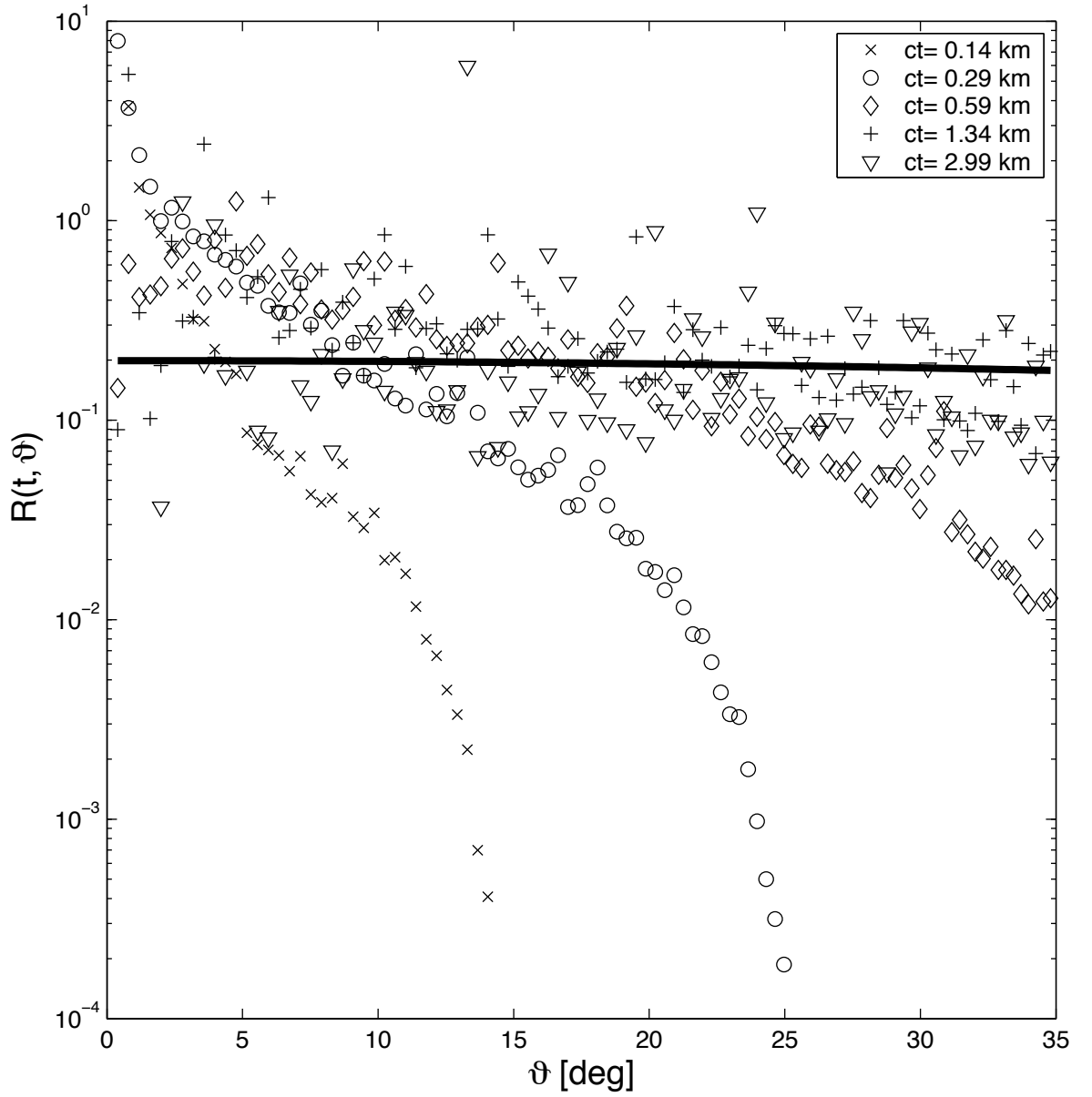
igure 7: Ratio $R(t, \theta)$ in E . (12) as a function of the obser ation angle θ for se eral alues of ct. The strict di usion prediction $u(\cos\theta)$ in E . ( ) is sho n by the solid line. The cloud optical thickness is 20 and its geometrical thickness is 0.7 km distance to the cloud is 0.5 km. The phase function is Deirmend ian Cloud C.1. The early times ($ct < 1$ km) here ( ) fails systematically ere not used in our retrie als of dense cloud properties.
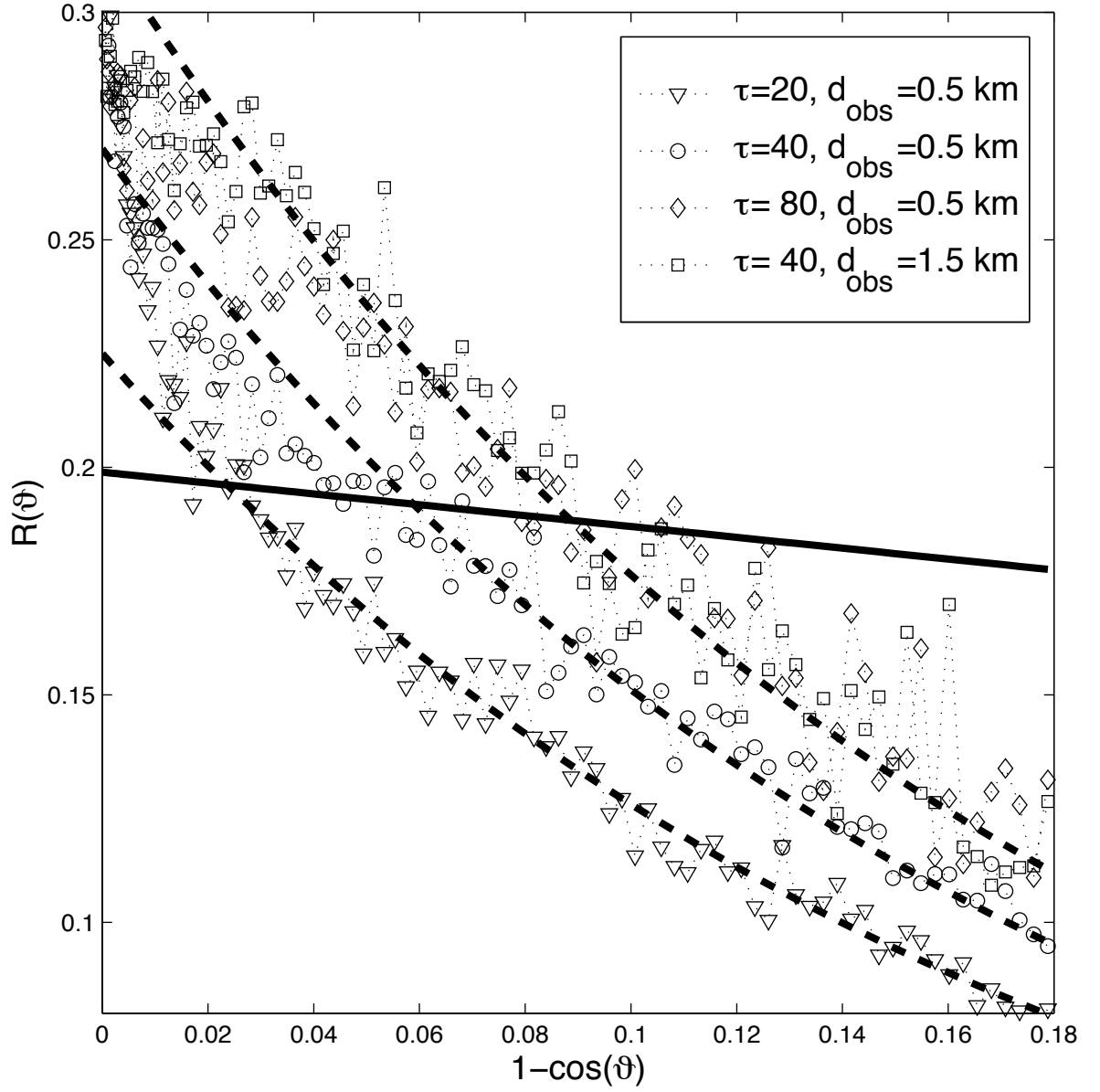
igure : Ratio $R(\theta)$ in E . (13) as a function of $1 - \cos\theta$ for se eral alues of the cloud optical and distance to the cloud. Cloud thickness is held constant at 0.7 km and the phase function is Deirmend ian model Cloud C.1. The strict di usion prediction $u(\theta)$ in E . ( ) is sho n by the solid line. The dashed lines depict our empirical radiance-to- u correction factor in E . (14).
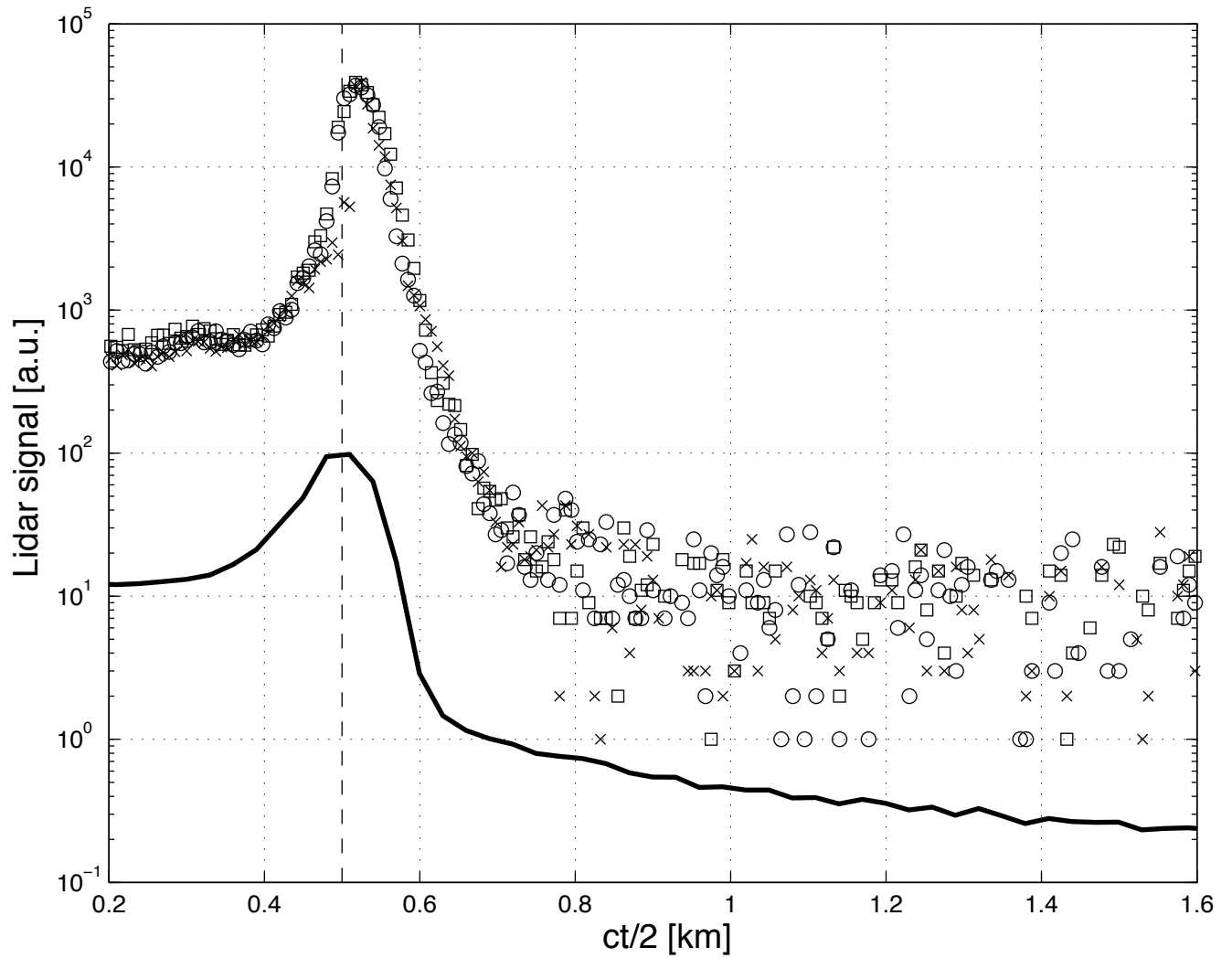
4

igure : T he lidar signal measured by the central WA L pi el as a function of range from the ground. Symbols correspond to di erent measurement times: 7:23 ( ), 7:52 (o), and 7:5 (□) in T C . T he ertical dashed line marks 0.5 km range here WA L and other instruments detect cloud base. T he solid black line sho s the MPL signal detected at :00 T C. t sho s ho the MPL sees a cross-o er from the aerosol background to cloudy air at a some hat shorter range than the estimate from the WA L data (based on the homogeneous slab assumption).
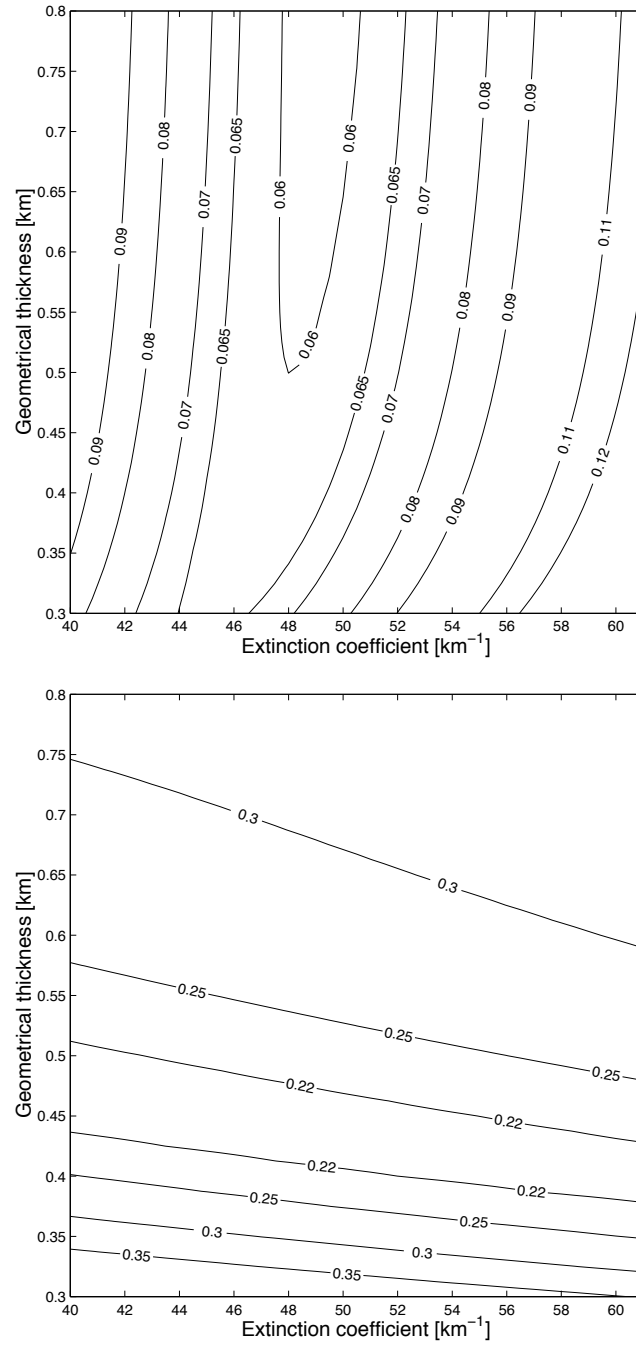
Figure 10: Cost function for tting the WA L signal detected at 7:30 T C using di usion formulas: the time-integrated case (upper panel) and the time-resol ed case (lo er panel). urther details in the te t.
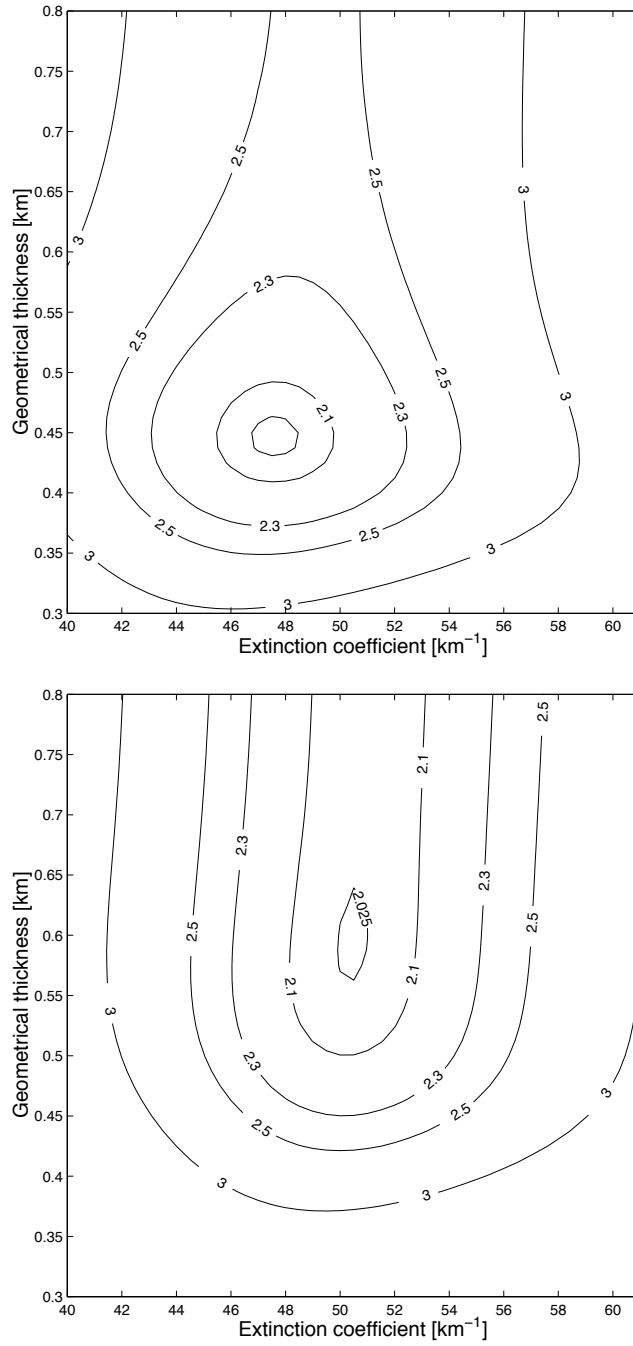
Figure 11: Merged cost functions for fitting WASL signals detected at 7:30 UTC (upper panel) and at 8:00 UTC (lower panel). For the upper panel, the components are obtained from those of Fig. 10, normalized by their minima.
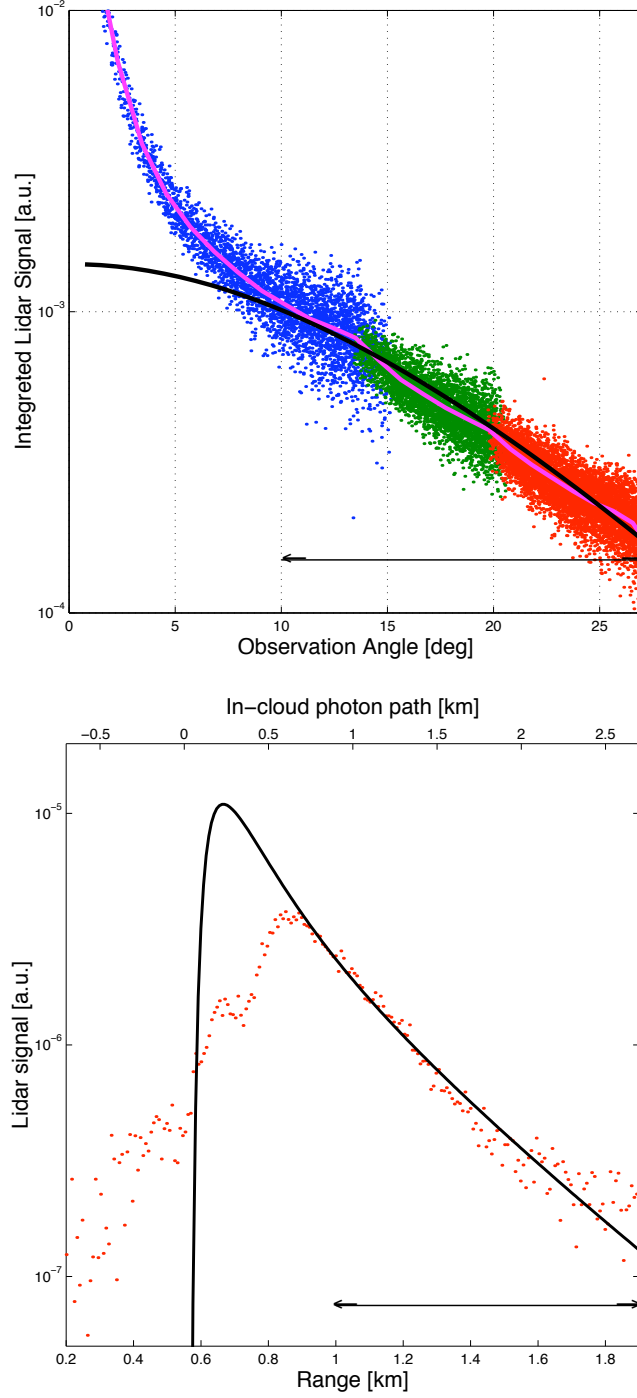
Figure 12: Upper panel: Time-integrated flux density as a function of the observation angle θ. The dots of 3 different colors correspond to WAIL radiance measurements at 7:30 UTC through the 3 interference filters in Fig. 2 and converted to flux using the empirical factor in (14). The solid black line is the best fit steady-state diffusion model in Eq. (10) using parameters from the corresponding panel in Fig. 11. The colored line is a running mean of the WAIL data that approximates that used in the regression (that used azimuthal averages) where we plot WAIL pixel values to show their spread from natural variability as well as instrumental noise. Lower panel: Time-resolved flux density as a function of range and in-cloud path for the narrow annulus of pixels at $\theta = 26.6°$. The
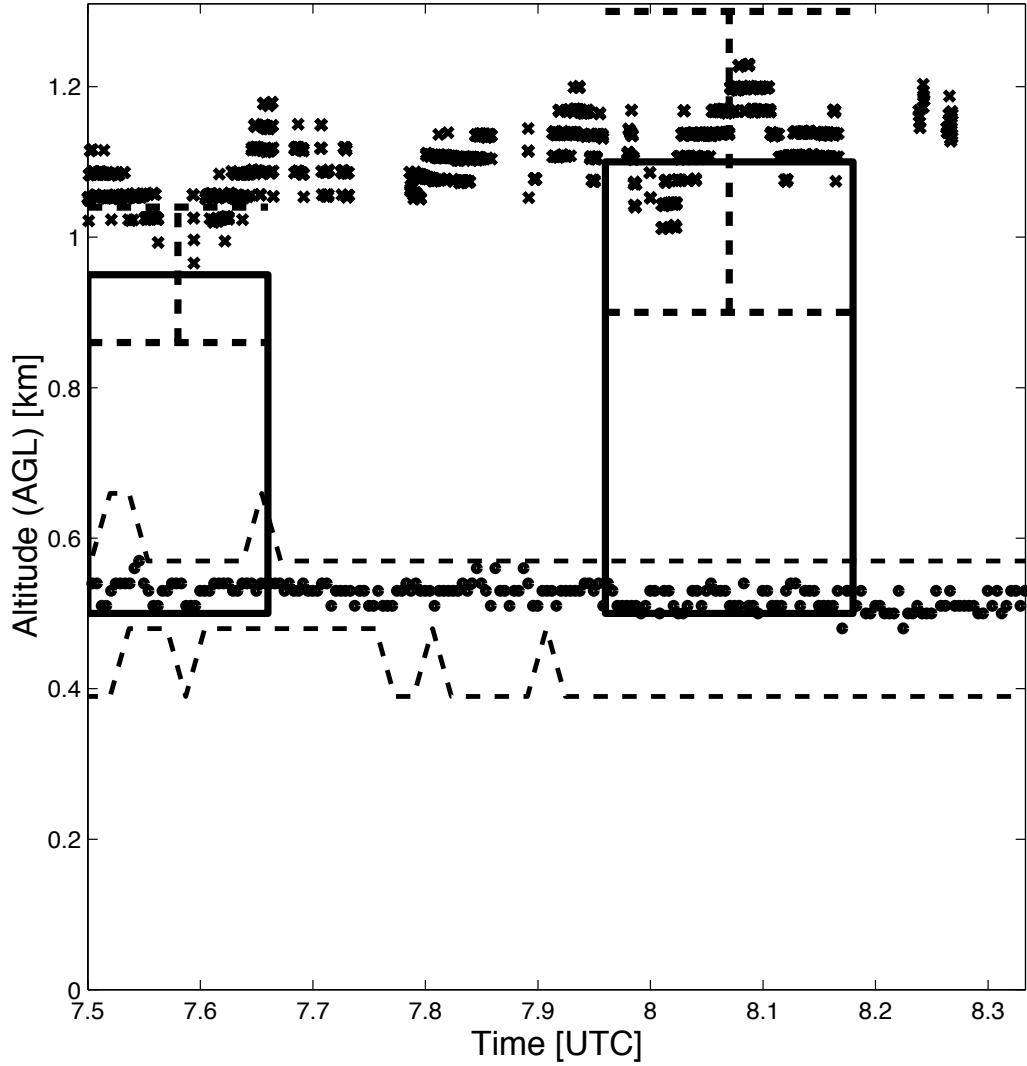
igure 13: Cloud-base and cloud-top heights as a function of time. The dashed lines sho the heights of cloud base and top retrie ed from the MPL data. The MPL cloud-top data is not reliable in the present case of an optically thick layer. The dots deri e from the ceilometer. The time-series for cloud top indicated by symbols is from the THOR instrument (courtesy T. Varnai and . etzer) that instrument as bet een 1 and 40 km a ay from the central facility (measured horizontally) during this time period. A t 7.3 T C THOR as at its closest (0.3 km horizontally) and then estimated the cloud-top height to be 1.07 km. Our collection periods and retrie als of the cloud-base and -top altitude are sho n by the rectangular areas hile the dashed lines depict uncertainties in the cloud top estimation. 54
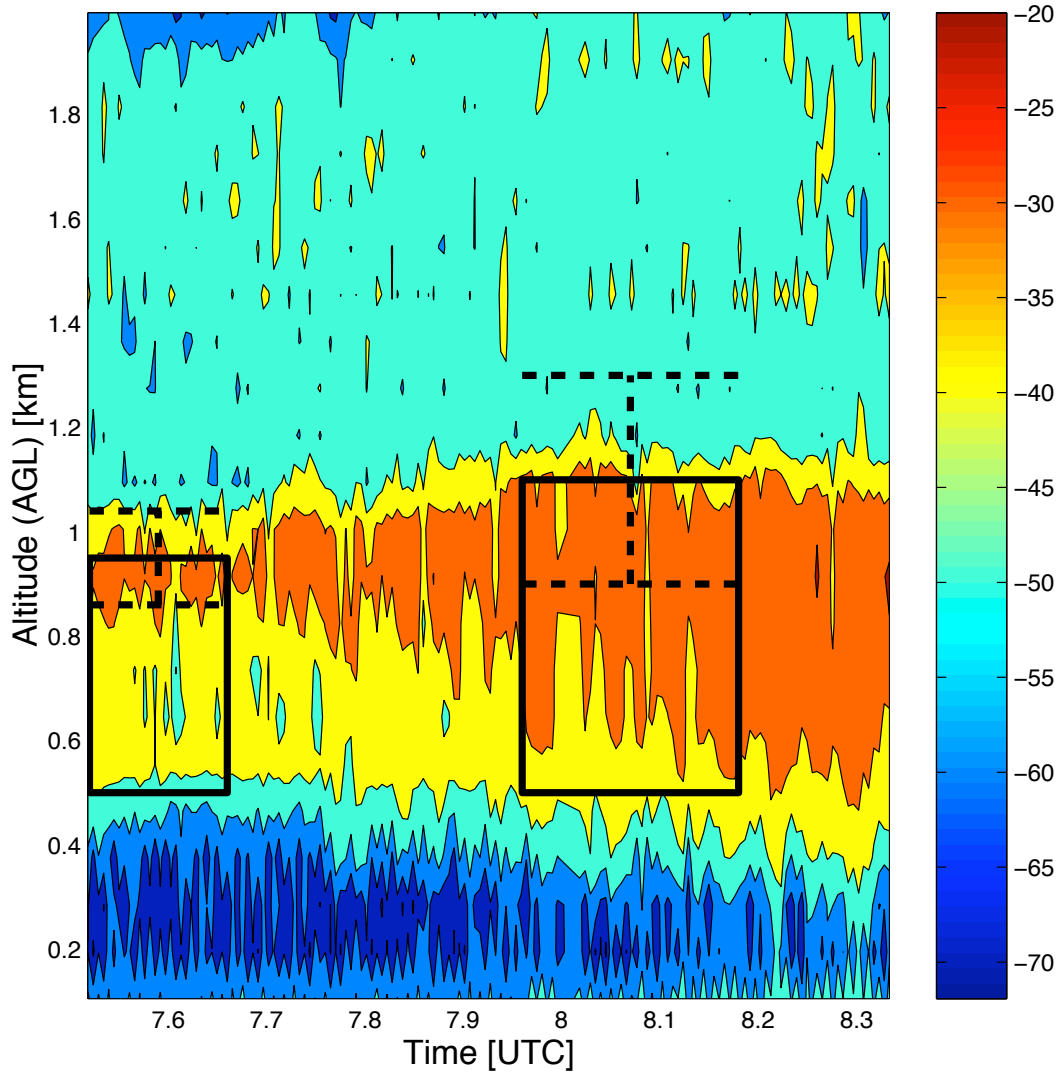
igure 14: Cloud re ecti ity (in dB) as a function of time and altitude abo e ground le el (AGL) retrie ed from the MMCR data. The layer ith a strong re ecti ity is situated bet een appro i- mately 0.4 km and 1.1 km. The rectangles sho the location of the cloud inferred from WA L data (and the duration of the 3- lter collection) hile the dashed lines depict uncertainties in the cloud top estimation.
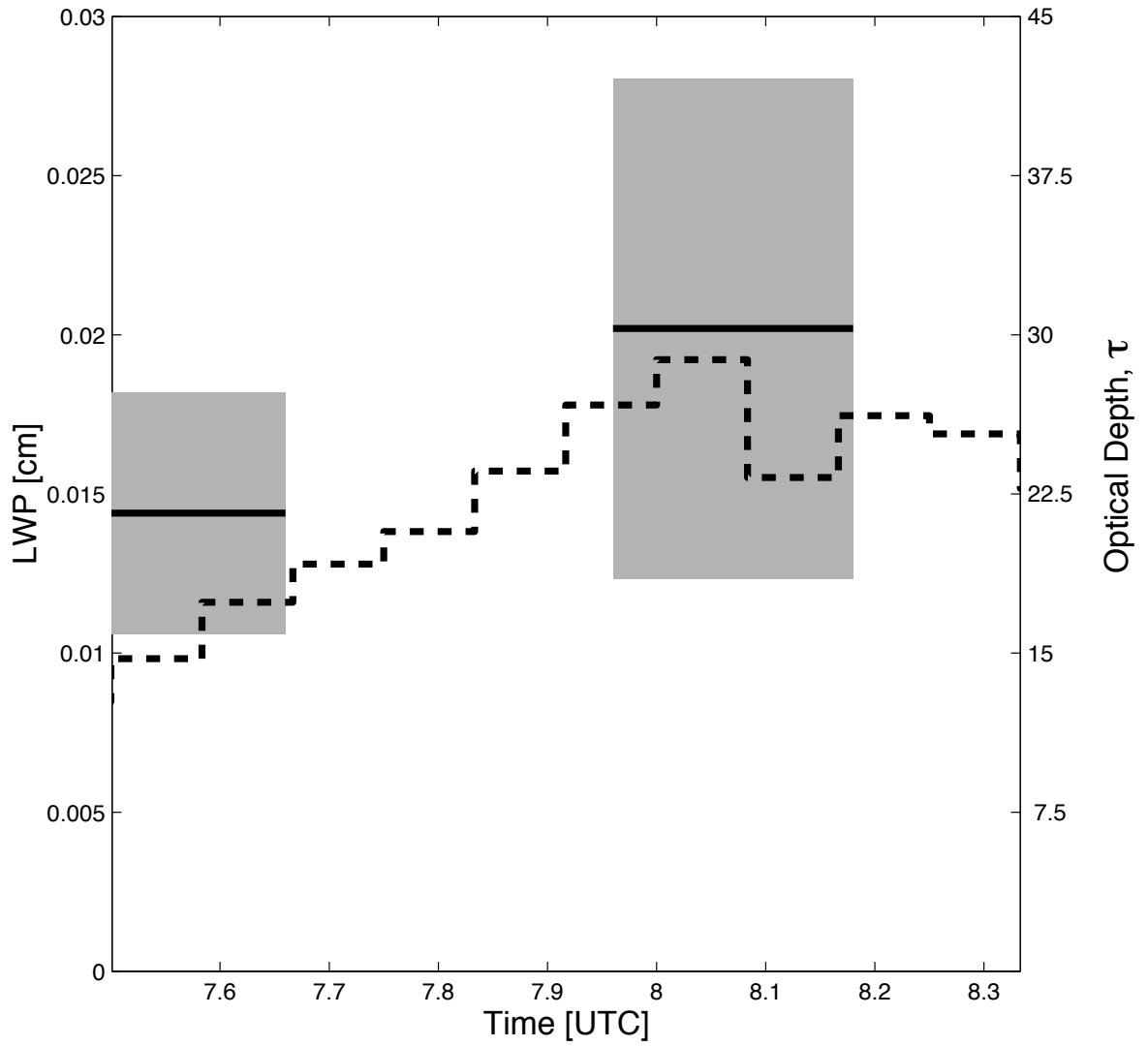
igure 15: Li uid ater path LWP (left a is) and cloud optical thickness (right a is) as a function of time. The estimation of the optical thickness from the MWR data (dashed line) may ha e as much as 20   error due to uncertainty of the e ecti e droplet radius (set here to 10 μm for simplicity). The horizontal solid lines sho   the optical thickness and associated LWP from the WA L data   hile the grey patches sho   the estimation error.